Late Paleozoic oceanic basalts hosted by the Char suture-shear zone, East Kazakhstan: Geological position, geochemistry, petrogenesis and tectonic setting

I.Yu. Safonova [a,b,*], V.A. Simonov [a], E.V. Kurganskaya [a], O.T. Obut [c], R.L. Romer [d], R. Seltmann [e]

[a] Sobolev Institute of Geology and Mineralogy SB RAS, Koptyuga Ave. 3, Novosibirsk 630090, Russia
[b] Korean Institute of Geoscience and Mineral Resources (KIGAM), 92 Gwahang-no, Daejeon 305-350, Republic of Korea
[c] Trofimuk Institute of Petroleum Geology and Geophysics SB RAS, Koptyuga Ave. 3, Novosibirsk 630090, Russia
[d] Deutsches GeoForschungsZentrum (GFZ), Telegrafenberg, D-14473 Potsdam, Germany
[e] Natural History Museum, Centre for Russian and Central EurAsian Mineral Studies (CERCAMS), Cromwell Road, London SW7 5BD, UK

ARTICLE INFO

ABSTRACT

The paper presents the first data on geochemistry (major and trace elements, isotopes) of the Late Devonian–Early Carboniferous basalts of the Char suture-shear zone in East Kazakhstan, and includes detailed analysis of their geological relations and petrogenesis (fractional crystallization/melting modeling). Three groups of oceanic basalts coexist in the Char zone. Group 1 basalts are associated with oceanic siliceous sediments and have medium TiO_2, relatively flat REE patterns ($La/Sm_n = 0.7$, $Gd/Yb_n = 1.3$), $Zr/Nb_{av.} = 42$ and $\varepsilon Nd_{av.} = 6.3$. They formed at high degrees of melting of a depleted mantle source and were erupted in a mid-oceanic ridge setting. Group 2 basalts are associated with both chert and carbonate and have higher TiO_2, Hf, Y, Zr and P_2O_5 than the rocks of Group 1. They are similarly characterized by low Nb ($Nb/La_{pm} < 1$) and flat REE patterns ($La/Sm_n = 0.6$, $Gd/Yb_n = 1.1$), $\varepsilon Nd_{av.} = 8.3$, and $Zr/Nb = 44$. Group 2 basalts originated under lower degrees of melting than Group 1 basalts from a depleted mantle source, and possibly formed in a subducting oceanic plateau setting. Group 3 basalts are enriched in incompatible elements, i.e. have high LREE ($La/Sm_n = 1.8$), differentiated HREE ($Gd/Yb_n = 2.3$), Nb positive anomalies in the multi-element diagrams ($Nb/Th_{pm} = 1.5$, $Nb/La_{pm} = 1.1$), low Zr/Nb ratio ($\sim$9) and lower $\varepsilon Nd_{av.} = 4.6$. They formed at lower degrees of melting, compared to Groups 1 and 2, from a heterogeneous mantle source in the spinel ($Gd/Yb_n < 2$) and garnet ($Gd/Yb_n > 2$) stability fields. They possibly represent fragments of oceanic islands/seamounts formed in relation to mantle plume.

© 2011 Elsevier Ltd. All rights reserved.

1. Introduction

Several orogenic belts located in East Kazakhstan and adjacent regions of the Russian–Chinese–Mongolian Altay and Kyrgyz Tien Shan mountains are parts of the Central Asian Orogenic Belt (CAOB), also termed the Altaids, which formed in place of the Paleo-Asian Ocean (PAO). The CAOB is a huge Phanerozoic accretionary orogenic belt bounded by the Siberian Craton to the north and the Tarim and North China Cratons to the south (Zonenshain et al., 1990; Sengör et al., 1993). It hosts a large number of mineral deposits (Yakubchuk, 2004; Seltmann et al., 2010). The CAOB formed by early Neoproterozoic to late Paleozoic subduction–accretion processes, which resulted in the accretion of island arcs, ophiolites, supra-subduction units, and terranes with Precambrian crystalline basement to the southern margin of the Siberian Craton (e.g., Sengör and Natal'in, 1996; Badarch et al., 2002; Buslov et al.,

2001, 2004a; Kröner et al., 2007; Windley et al., 2007; Xiao et al., 2010; Rojas-Agramonte et al., 2011; Glory et al., 2011; Kröner et al., 2011). These various terranes and their geodynamic affinities are critical for reconstructing the tectonic evolution of the CAOB. Of special importance are terranes with ophiolitic/oceanic crust that mark suture-shear zones (SSZ) that formed after the closure of the PAO and the subsequent collision of continental blocks (e.g., Dobretsov et al., 1995; Buslov et al., 2001; Li, 2006). These SSZs, formerly also referred to "ophiolitic belts" or "strike-slip zones", occur in many segments of the CAOB (e.g., Polyanskii et al., 1979; Ryazantsev, 1994; Li, 1995; Buslov et al., 2001, 2004b; Badarch et al. 2002; Xiao et al., 2003).

Suture-shear zones often contain units of Oceanic Plate Stratigraphy (OPS; Isozaki et al., 1990, 2010; Santosh et al., 2009; Santosh, 2010), which include both sedimentary and volcanogenic rocks. OPS is characterized by a regular change of lithologic facies from mid-oceanic ridge basalts (MORB), pelagic (radiolarian-/ribbon/bedded chert), through oceanic island/seamount basalt (OIB), hemipelagic or slope facies (siliceous-lime shale and mudstone, carbonate breccia) and shallow-water carbonates (massive or micritic reefal limestone capping OIB) to terrigenous environment.
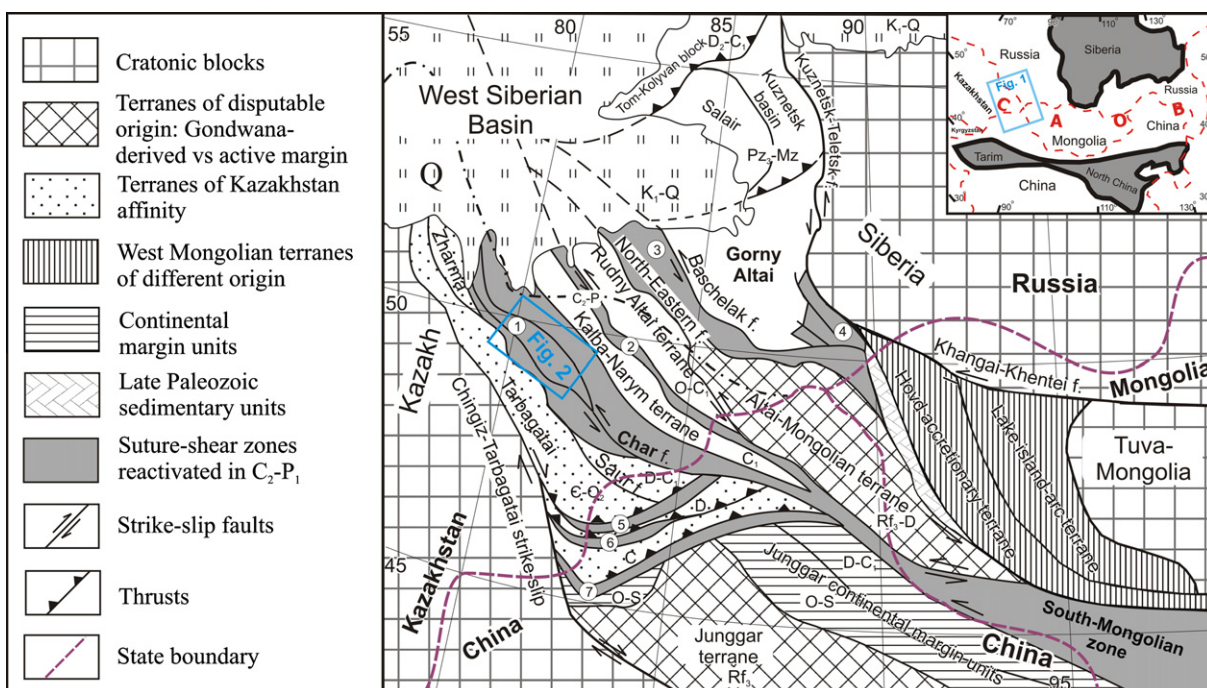
Fig. 1. Suture-shear zones reactivated in the Late Paleozoic: 1 – Char, 2 – Irtysh, 3 – Charysh-Terekta, 4 – Kurai, 5 – Barlik-Khongulen-Khebukesair, 6 – Mailskaya, 7 – Dalabute. Abbreviations: f – fault. Modified from Buslov et al. (2004b).

OPS units are incorporated into accretionary complexes during subduction of oceanic plate, which, after oceanic closure, become parts of suture-shear zones. Chert and carbonate may contain microfossils (radiolaria, conodonts), which often represent the only possibility to determine the age of oceanic units. Most mafic rocks experienced strong post-magmatic sea-floor hydrothermal alteration and later accretion-related deformation. During subduction, fragments of OIB may be incorporated into accretionary complexes, whereas MORB mostly submerged into the upper mantle. Thus, OPS units, which include oceanic floor (MORB) and oceanic island (OIB) basalts, provide unique insights into the geodynamic development of orogenic belts formed in place of former oceans.

The Char or Chara suture-shear zone of East Kazakhstan is an important segment of the CAOB (Fig. 1). It is special for its extremely complicated tectonic structure and co-occurrence of ultramafic–mafic ophiolitic units, various volcanosedimentary sequences, and Paleozoic basaltic lavas (e.g., Polyanskii et al., 1979; Ermolov et al., 1981; Belyaev, 1985; Buslov et al., 2001; Dobretsov, 2003). Its study is important for reconstructing the geodynamic history of the western parts of the CAOB including vast folded areas in East Kazakhstan, southern Siberia, northeastern China and western Mongolia. The Char zone hosts Late Devonian–Early Carboniferous units of OPS (Iwata et al., 1994, 1997; Sennikov et al., 2003; Safonova et al., 2009). Earlier studies of the OPS sedimentary units in the Char SSZ focused on the general geology, tectonics, and lithology (Polyanskii et al., 1979; Ermolov et al., 1981; Belyaev, 1985; Buslov et al., 2001), to a lesser extent, on geochemistry of oceanic basalts (Safonova et al., 2004, 2009). This paper presents new detailed data on the major and trace element and isotope geochemistry of basalts, which will contribute to our understanding of their petrogenesis, mantle sources, and geodynamic origin.

2. Geological setting of OPS units

The Char SSZ, which was referred to as Chara ophiolitic belt in Buslov et al. (2001) and as Chara strike-slip zone in Buslov et al.

(2004b), is located between two island-arc zones: the Rudny Altai in the northeast and the Zharma-Saur in the southwest (Berzin et al., 1994) (Fig. 1). The Char zone marks the final stage of the evolution of the Paleo-Asian Ocean and is the main suture related to the collision and amalgamation of the Kazakhstan and Siberian continents (e.g., Polyanskii et al., 1979; Ermolov et al., 1981; Belyaev, 1985; Dobretsov, 2003; Sennikov et al., 2003; Buslov et al., 2001, 2004b). The zone experienced strong strike-slip faulting and shearing in the Late Carboniferous–Early Permian, which deformed island-arc, continental margin, and oceanic units. These deformations possibly were related to the collision of the Kazakhstan and Siberian continent and subsequent clockwise rotation of the latter (Didenko et al., 1994). Numerous displaced and mixed tectonic sheets of different geodynamic origin are present as tectonic mélanges. Three types of serpentinite mélange, comprising OPS and fragments of island arcs are recognized in the Char zone. Type I Early Paleozoic subduction melanges contain blocks of HP metamorphic rocks, gabbro and basalt in serpentinite matrix. Type II Ordovician ophiolitic melanges contain blocks and lenses of OPS units including serpentinized peridotite, gabbro, and amphibolite. Type III Late Carboniferous to Early Permian mélanges separate tectonic thrust sheets, which outline the Char zone (Figs. 2A and 3). The NW-oriented Type III mélanges coincide with the strike of the Char SSZ (Ermolov et al., 1981; Belyaev, 1985; Buslov et al., 2001, 2004b).

Basalts associated with OPS units, i.e., massive limestone, siliceous slope facies and pelagic chert, occur as tectonic sheets and blocks in Type III mélange (Fig. 4). Reconnaissance of geochemical investigations indicate that the Char basalts formed in oceanic ridge, oceanic island, and island arc geodynamic environments (Dobretsov, 2003; Buslov et al., 2001; Safonova et al., 2004, 2009) in the NE branch of the Paleo-Asian Ocean. They were accreted to the active margin of the Siberian continent during its Late Carboniferous collision with the Kazakhstan continent and subsequent ocean closure (Buslov et al., 2004b).

Fig. 2B shows a generalized stratigraphic pre-deformation section of the units included in the Char SSZ (Ermolov et al., 1981; Belyaev, 1985; Bykova and Kushev, 1974; Iwata et al., 1997). The
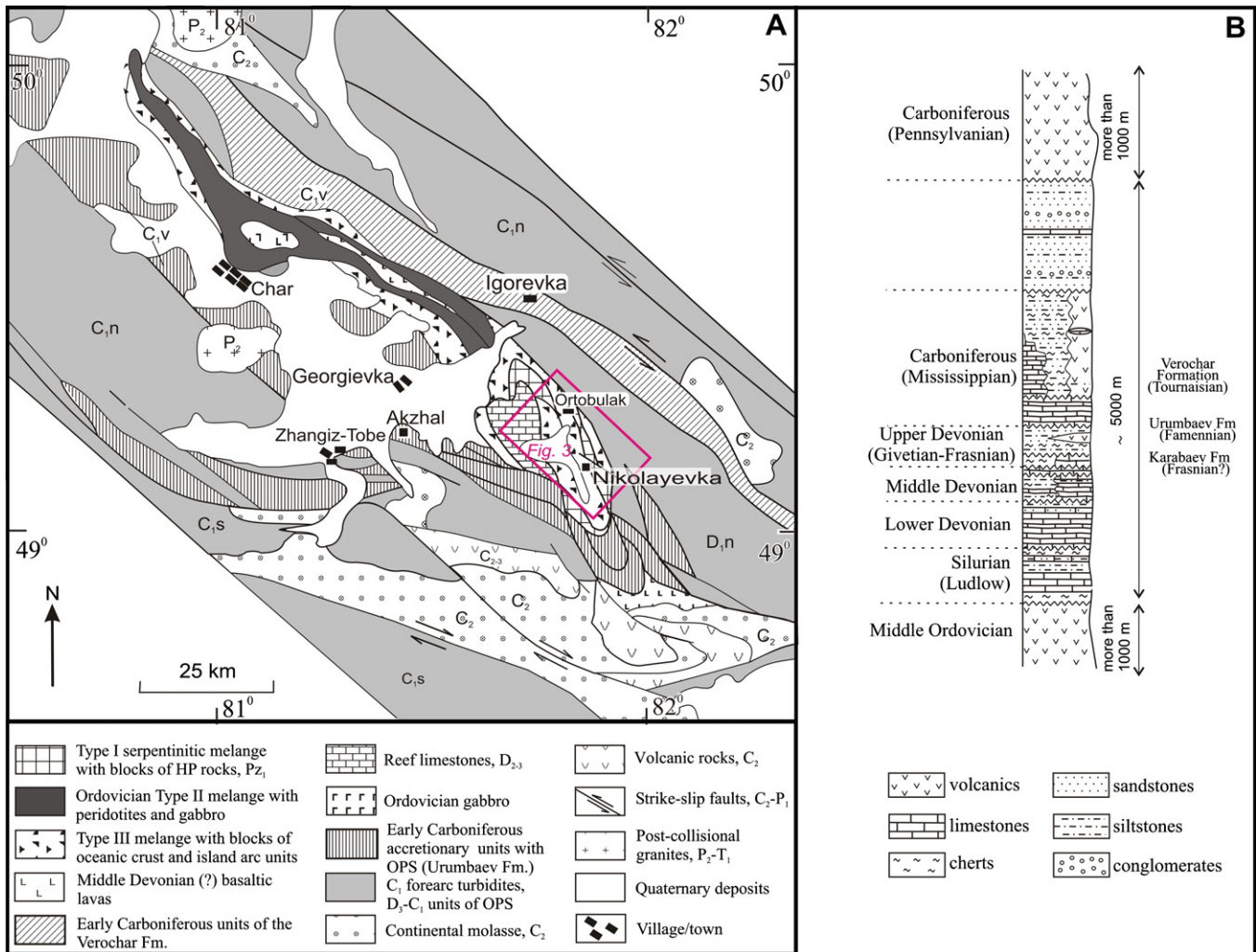
Fig. 2. (A) Geological map of the Char zone (modified from Ermolov et al. (1981)). (B) Generalized stratigraphic column of the Char SSZ with numerous accretion-related tectonic unconformities and possible reversals (generalized from Bykova and Kushev (1974), Ermolov et al. (1981), Belyaev (1985), and Iwata et al. (1997)).

sedimentary rocks from the mélanges contain Late Devonian to Lower Carboniferous radiolarians (Ermolov et al., 1981; Iwata et al., 1997; Sennikov et al., 2003). The cherts (Karabaev Fm.) contain Late Devonian radiolarians, whereas limestones intercalated with siliceous sediments (Verochar Fm.) host Early Carboniferous radiolarians (Fig. 2B; Iwata et al., 1997; Sennikov et al., 2003). This agrees well with the general model of OPS implying that pelagic sediments may be both younger and older than the shallow-water seamount top carbonates (Isozaki et al., 1990).

In terms of "classic" stratigraphy, all units, formations and sequences have tectonic contacts and older blocks could be incorporated into younger strata as olistolites. The age of the sedimentary rocks was established by graptolites, radiolarians, brachiopods, and foraminifers (Ermolov et al., 1981; Iwata et al., 1997). The Carboniferous olistostromes hosted by serpentine mélange include numerous blocks of Ordovician, Silurian and Devonian limestone and chert (Belyaev, 1985; Ermolov et al., 1981). The Paleozoic sequence starts with a Middle Ordovician volcanogenic-sedimentary unit (Fig. 2B) consisting of dolerite, andesitic porphyrite, jasper with subordinate siltstone and siliceous mudstone. This unit is unconformably overlain by Silurian (Llandovery-Ludlow) terrigenous siliceous shale, siliceous mudstone and sandstones intercalated with limestone. The Silurian section is unconformably overlain by thick Lower Devonian carbonates (biogenic limestone), Middle Devonian rhythmically alternated siliceous and siliceous-

carbonate mudstone, siliceous shale, sandstone, and chert and an Upper Devonian volcano-sedimentary unit, i.e., the Karabaev and Urumbaev formations. The pillow lavas together with associated oceanic sediments are regarded as fragments of ophiolites (Iwata et al., 1997).

In the Carboniferous section, the Early Mississippian volcanic-carbonate-terrigenous deposits are increasingly replaced by more coarse-grained terrigenous rocks. The Carboniferous biogenic limestones, cherts, and siliceous mudstones are associated with basalt, andesite, rhyolite, tuff and tuffeceous sandstone of the Verochar Formation (Tournaisian). The Verochar Formation is overlain at an unconformity by siltstone and sandstone with intercalated coal-bearing beds and conglomerates. The Mississippian volcano-sedimentary sequence is unconformably overlain by Pensylvanian basalt and porphyrite, tuff, and lava-breccia (Fig. 2B).

The various tectonic sheets and blocks have been displaced along strike-slip faults by tens or possibly hundreds of kilometers, resulting in doubling or omissions in local lithostratigraphic sections. The Late Devonian–Early Carboniferous rock packages show that most OPS units (e.g., basalts, cherts, siliceous mudstone and shale, slope facies) have tectonic contacts (Fig. 2B).

Samples of basalts for geochemical study were regionally distributed, preferably from sections exposing the basalt-sediment contact (Fig. 4), along the Char River and its tributaries, near Char, Akzhal, Georgievka (Kalbatau), Nikolayevka, Zhangiz-Tobe,
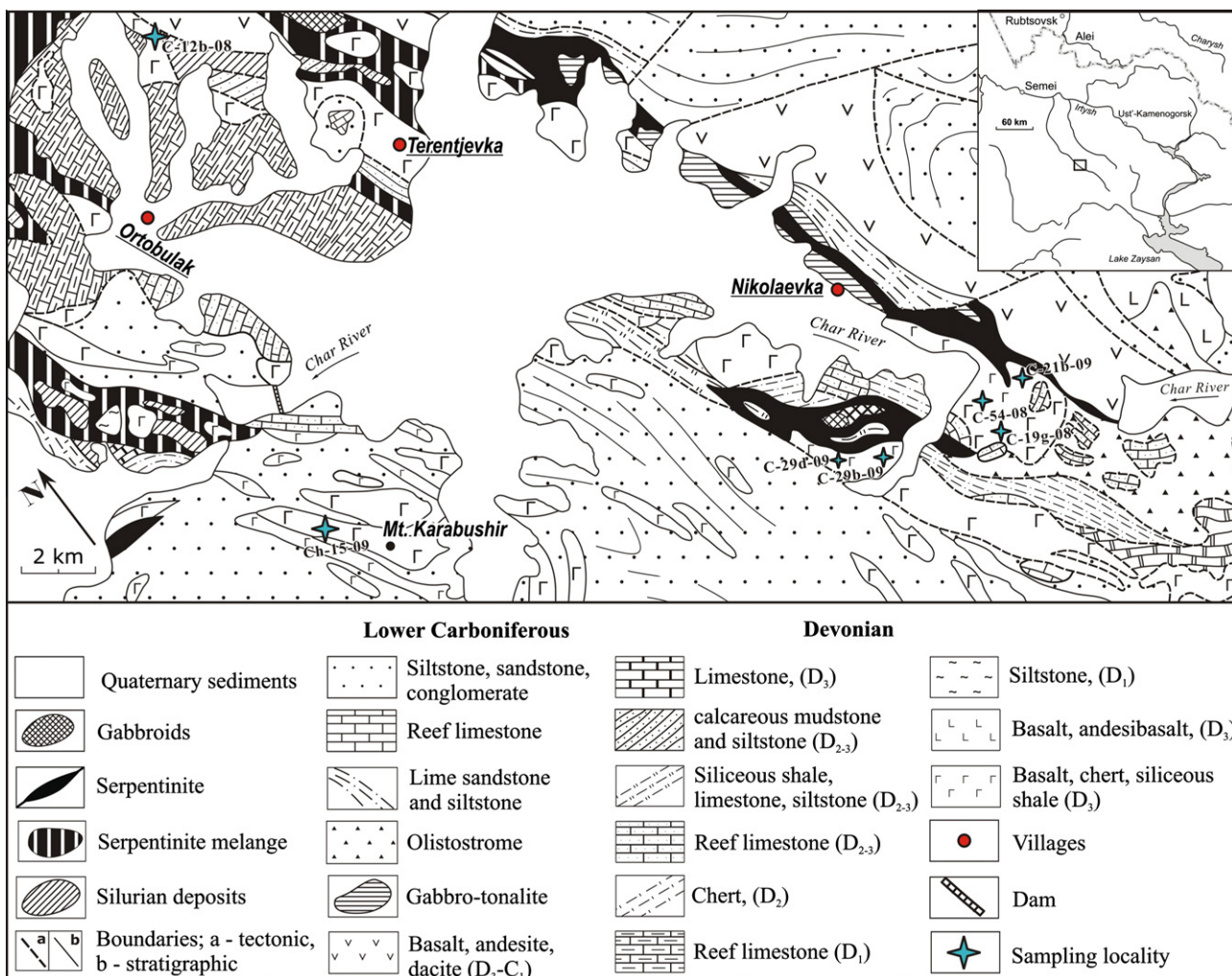
Fig. 3. Schematic geological map of the area between the dam across the Char River and Nikolaevka Village showing a complicated structure and several sampling localities (modified from Polyanskii et al. (1979)).

Ortobulak, Terentyevka and Igorevka Villages, Karabushir Mt., and near the dam across the Char River (Figs. 2–4; Table 1). There, the Late Devonian–Early Carboniferous basalt-sedimentary units alternate with tectonic sheets of Visean–Serpukhovian olistostromes (Belyaev, 1985; Sennikov et al., 2003). In the Char site, the OPS units (chert) contain Early Carboniferous radiolarians (Iwata et al., 1997). In the Nikolaevka site, a sample of limestone taken close to a basaltic unit carrying Late Devonian conodonts (unpublished data).

The composition and geodynamic settings of several samples of basalts were briefly discussed before (Buslov et al., 2001; Safonova, 2009; Safonova et al., 2004, 2009). In the present paper, the petrogenetic and tectonic implications are based on the field relations of volcanogenic units, their verified geological setting, and detailed analysis of their geochemistry, i.e., major, trace and rare-earth elements and isotopes.

3. Petrology

Volcanic rocks from the Urumbaev, Verochar, and Karabaev formations (Fig. 2A and 3; see Section 2) are porphyric and amygdaloidal basalts, diabases and basaltic andesites (Table 1; Fig. 5). Basaltic andesites have porphyric texture and massive structure. The phenocrysts are sericitized plagioclase (70%) of 0.5–2 mm length. The groundmass is pilotaxitic and consists of subparallel plagioclase microliths and fine-distributed opaque grains (30%).

Basalts are porphyric, aphyric and amygdaloidal. The porphyric varieties have massive structure with euhedral to subhedral phenocrysts of albitized plagioclase (1–3 mm), clinopyroxene (0.3–0.5 mm) and magnetite (<0.5 mm) phenocrysts. The groundmass is microlithic, pilotaxitic or intersertal; it consists of plagioclase laths (30–60%), opaque minerals (15–30%), volcanic glass (30%), and isometric grains of pyroxene (up to 10%). Radial aggregates of green chlorite locally replace volcanic glass. The aphyric basalts consist of strongly altered plagioclase laths (30–60%), pyroxene (<20%), glass (<5%), and opaque minerals (10–15%) and are cut by 0.1–1 mm thick quartz veinlets. In amygdaloidal varieties, the amygdules are filled by prehnite, quartz and calcite. There are abundant secondary minerals: chlorite, epidote, pumpellyite, chalcedony, and iron hydroxides.

The rocks experienced low-temperature metamorphism at greenschist facies conditions. Our study mainly focuses on the whole rock geochemical characteristics as primary olivine, pyroxene, and plagioclase are strongly altered.

4. Methods

Twenty-one representative analyses of Char mafic volcanics were selected for detailed geochemical characterization including two published in (Safonova et al., 2009) (Table 1). The rock samples were first split into small chips, then hand-picked under binocular
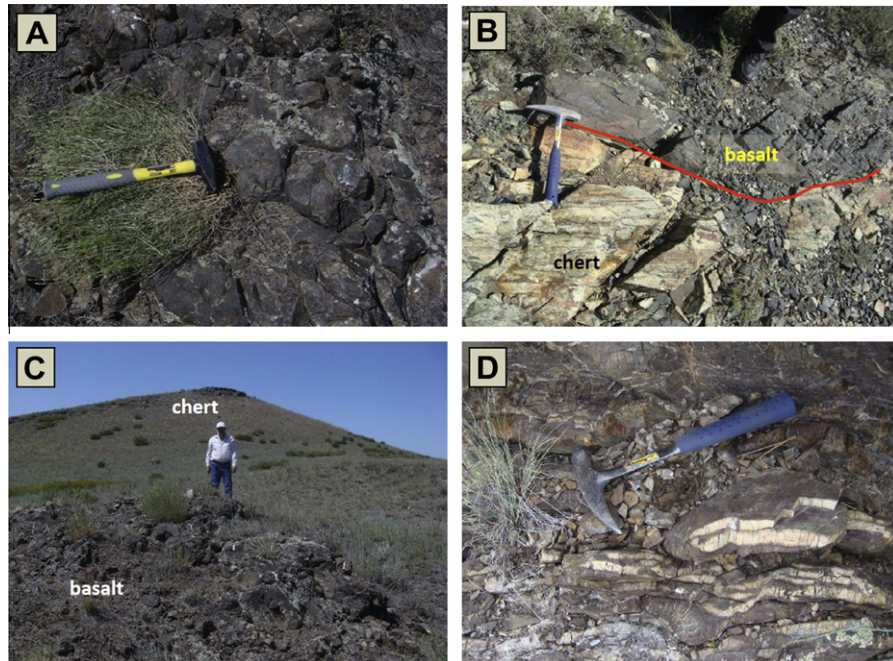
Fig. 4. Photographs of field occurrences and contacts of basalts and oceanic sediments: (A) "micro" pillow lava (Char site); (B) OIB-type basalt contacting gray chert (Zhangiz-Tobe site); (C) MORB-type basalt contacting brown chert (Char site); (D) ribbon chert (Nikolaevka zite).

Table 1
Description of samples from the Char suture-shear zone.

Group/sample no.	Rock type	Mode of occurrence	Location	Coordinates
Group 1 (depleted): low-Ti–Nb–LREE				
C-12b-08	Dolerite	Lava flow	Ortobulak	N49°17′29.6″; E81°50′45.1″
95-94[a]	Basalt	Lava flow	Akzhal	–
Ch-54/1-08	Amygdule basalt	Lava flow	Nikolaevka	N49°10′00.3″; E81°57′29.7″
Ch-08-09	Diabase	Pillow-lava	Nikolaevka	N49°36′01.9″; E81°01′07.5″
C-21b-09	Aphyric basalt	Pillow-lava	Nikolaevka	N49°06′30.2″; E82°00′01.0″
Group 2 (transitional): high-Ti, low Nb–LREE				
Ch-15-09	Aphyric basalt	Lava flow	Karabushir Mt.	N49°11′43.4″; E81°47′22.1″
Ch-23-09	Porphyric basalt	Lava flow	Zhangiz-Tobe	N49°11′35.4″; E81°11′27.2″
Ch-28-09	Dolerite	Lava flow	Zhangiz-Tobe	N49°11′36.0″; E81°11′28.0″
C-25b-09	Porphyric basalt	Lava flow	Zhangiz-Tobe	N49°11′30.0″; E81°11′32.0″
Ch-20-08	Porphyric basalt	Lava flow	Zhangiz-Tobe	N49°11′36.9″; E81°11′28.2″
C-19g-08	Aphyric basalt	Pillow-lava	Nikolaevka	N49°06′23.1″; E81°59′58.4″
97-106	Porphyric basalt	Pillow	Char	–
97-116	Aphyric basalt	Pillow	Char	–
97-117	Aphyric basalt	Pillow	Zhangiz-Tobe	–
97-118	Aphyric basalt	Pillow	Zhangiz-Tobe	–
Group 3 (enriched): high-Ti–Nb–LREE				
97-119-3	Aphyric basalt	Pillow-lava	Igorevka	–
C-29d-09	Aphyric basalt	Pillow-lava	Nikolaevka	N49°07′17.5″; E81°57′33.6″
C-29b-09	Porphyric basalt	Lava tube	Nikolaevka	N49°07′19.5″; E81°57′26.6″
C-26g-09	Porphyric basalt	Lava flow	Char	N49°33′29.6″ E81°26′35.9″
97-101	Porphyric basalt	Lava flow	Char	–
97-102	Dolerite	Dike	Char	–

[a] Samples taken in 1995 and 1997 have no precise geographic coordinates, because no GPS device was available at that time.

to avoid fragments with carbonates and clay minerals and finally ground in an agate or ceramic mill.

4.1. Major and trace elements

Abundances of major elements in all samples were determined at the Institute of Geology and Mineralogy SB RAS by X-ray fluorescence spectrometry (XRF) using a "Nauchpribor" device. The analytical procedure followed the Russian analytical standard OST-41-08-212-82 Mingeo SSSR; relative standard deviations (RSD) are within 5%, and totals were within 100 ± 1%. Trace elements in

samples Ch-xx-08, Ch-xx-09, C-xx-08 and C-xx-09 (Table 2) were analyzed by inductively coupled plasma mass-spectrometry (ICP-MS) in the Institute of Geology and Mineralogy SB RAS (Finnigan Element ICP-MS) using the protocols of Jenner et al. (1990). Powdered samples were dissolved using a HF-HNO$_3$ (2:1) mixture in a screw-top Teflon beaker for 2 days at ~100 °C followed by evaporation to dryness, refluxed in 6 N HCl and dried twice, and then re-dissolved in 1 N HCl. The procedure was repeated until the powder was completely dissolved. The final solution was evaporated to dryness, refluxing in 6 N HNO$_3$ and drying three times, and dissolved in 2% HNO$_3$. Wet chemical procedures were conducted
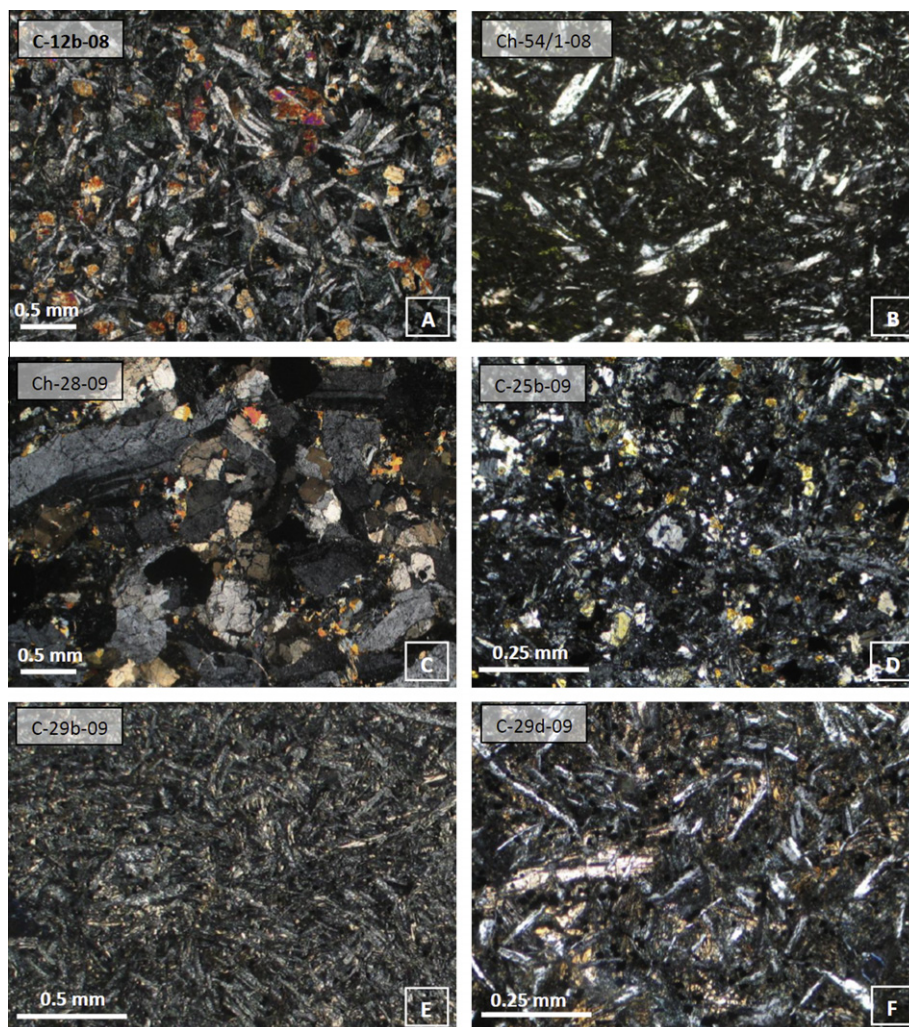
Fig. 5. Photos of thin sections of Char basalts (for petrographic types see Table 1 and the text, Section 3). (A and B) Group 1; (C and D) Group 2; (E and F) Group 3 (see text and Tables 2 and 3 for grouping details).

under clean lab conditions. BHVO-1 (Jenner et al., 1990), BCR-1 (Jochum and Nohl, 2008) and JB-3 (Orihashi and Hirata, 2003) were used as international reference materials to estimate precision and accuracy. The analytical errors are estimated as 2–7% for rare earth elements (REE) and high-field strength elements (HFSE).

Abundances of HFSE, REE, large-ion lithophile elements (LILE) and major elements (Na, Ca, Fe) in samples 97-xx and 95-94 (Table 2) were determined by instrumental neutron activation analysis (INAA) using Ge detectors for γ-rays higher that 30 keV and below 2000 keV. The samples were radiated using a nuclear reactor of the Tomsk Polytechnical University by an integral flux of 10^{17} neutrons/cm². The measurements were made on a gamma-spectrometer in two cooling stages of 1 week and 3 months. The concentrations of Y, Zr, Nb, Ti, Rb, Sr, Pb, V, Mn, Ni, Cu, Zn were also determined by SR XRF (synchrotron radiation XRF) (Phedorin et al., 2000).

For chondrite normalized (e.g., La/Sm$_n$) and primitive mantle (PM) normalized (e.g., Th/Nb$_{pm}$) data presentation, we used the values of Sun and McDonough (1989). Zr/Zr*, Hf/Hf* and Eu/Eu* ratios were calculated with respect to the neighboring immobile elements, following the method of Taylor and McLennan (1985), normalized to chondrite (Eu) and primitive mantle (Zr, Hf), respectively. Samples were recalculated to 100% anhydrous for intercomparisons. Mg-numbers (Mg#) were calculated as the molecular ratio of Mg/(Mg + Fe^{2+}) assuming 10%Fe^{3+}, which corresponds to

low-pressure crystallization conditions for oxygen fugacity of $\sim$FMQ-1.

4.2. Isotopes

The Sr, Nd, and Pb isotopic compositions were determined at Deutsches GeoForschungsZentrum (Potsdam) using MAT262 and Triton multi-collector mass-spectrometers, respectively. Samples for isotope analysis were dissolved with concentrated HF for 4 days at 160 °C on the hot plate. Digested samples were dried, taken up in 2 N HNO₃, and dried at low temperatures over night to convert fluorites into nitrates. The samples were re-dissolved in 6 N HCl and split by weight into three fractions, one for the isotopic composition of Sr and Nd, one for the isotopic composition of Pb, and one to determine the concentrations of Pb and U by isotope dilution. Sr, Nd, and Pb were separated and purified using ion-exchange chromatography. For details see Romer et al. (2005) and Romer and Hahne (2010).

5. Results

There are three groups of basaltic samples, which have different major and trace element characteristics (Tables 2 and 3). According to SiO₂ and total alkali (Na₂O + K₂O) contents the samples are basalt, andesitic basalt and trachybasalt (Fig. 6A). In the SiO₂ versus

Table 2
Major oxides (wt.%) and trace elements (ppm) in basalts of the Char SSZ.

Sample	1 C-12b-08	2 95-94	3 Ch-54-08	4 Ch-08-09	5 C-21b-09	6 97-106	7 Ch-15-09	8 Ch-20-08	9 C-19g-08	10 C-25b-09	11 Ch-23-09
SiO_2	45.3	48.5	48.9	50.7	50.0	46.2	50.2	45.6	45.0	48.2	45.9
TiO_2	1.27	1.61	1.76	1.81	1.85	2.16	2.07	2.89	2.47	2.42	2.84
Al_2O_3	15.8	12.8	16.8	13.6	14.4	12.4	12.9	12.9	14.7	13.6	14.0
Fe_2O_3	13.0	11.5	12.7	12.6	13.8	13.6	12.6	17.0	14.9	14.9	18.2
MgO	7.71	6.48	5.4	7.3	7.53	5.62	5.38	6.24	6.7	6.49	5.17
CaO	9.07	12.4	6.29	7.34	4.38	10.95	9.93	10.25	10.25	80.8	4.88
MnO	0.17	0.21	0.26	0.19	0.13	0.2	0.19	0.24	0.18	0.21	0.27
Na_2O	4.46	2.68	3.17	3.26	4.20	3.4	2.20	1.98	3.06	2.68	3.34
K_2O	0.01	0.10	0.36	0.08	0.07	1.2	0.07	0.41	0.01	1.80	1.63
P_2O_5	0.06	0.13	0.2	0.16	0.18	0.21	0.20	0.35	0.25	0.22	0.28
L.O.I.	3.08	3.58	4.02	3.67	4.17	4.75	4.80	1.96	3.97	2.13	4.19
Total	99.9	99.7	99.9	100.7	100.7	100.6	100.5	99.9	99.8	100.7	100.7
Mg#	54	56	46	54	52	48	46	42	47	46	36
Rb	1.0	1.2	7.6	2	1.4	2.0	1.5	5.0	0.9	33.7	28.5
Sr	99	120	77	94	68	30	131	141	77	72	46
Y	23	32	28	37	42	41.2	44	52	50	54	65
Zr	65	92	127	121	137	150	177	207	126	194	204
Nb	2.0	2.0	1.8	3.4	4.7	3.5	3.1	3.6	5.6	4.3	5.1
Ba	13.4	68	78	37	31		24	62	55	114	142
La	3.8	4.2	5.3	3.6	3.0	4.7	4.3	5.8	6.7	5.1	4.9
Ce	8.3	12	11.3	9.9	9.5	14.3	13.1	15.2	15.1	14.9	16.2
Nd	8.1	10	11.5	9.8	9.8	13.0	12.9	17.6	16.6	14.1	16.2
Sm	2.9	3.2	4.4	3.5	3.6	5.2	4.4	6.5	5.7	4.9	5.6
Eu	1.3	1.5	1.6	1.1	1.1	1.8	1.5	2.3	2	1.5	1.7
Gd	4.7	5.5	5.4	4.6	4.9	7.2	5.5	7.9	7.6	6.6	7.7
Tb	0.6	0.7	0.8	0.9	0.9	1.3	1.0	1.3	1.3	1.2	1.4
Dy	4.1		5.8	5.9	6.2		6.7	9.3	9.4	7.8	9.2
Ho	0.8		1.2	1.2	1.3		1.5	2.2	2	1.7	2.0
Er	2.5		3.7	3.5	3.8		4.2	6.4	6.1	4.9	5.9
Tm	0.4		0.6	0.6	0.6		0.7	0.9	0.9	0.8	1.0
Yb	2.8	3.8	3.7	3.9	3.7	5.2	4.2	6.2	6.4	4.7	5.9
Lu	0.4	0.6	0.5	0.5	0.6	0.8	0.6	0.9	0.9	0.7	0.8
Hf	2.2	2.5	3.5	3.3	3.4	3.7	4.7	6	3.7	4.9	5.2
Ta	0.2	0.2	0.1	0.3	0.3	0.2	0.2	0.3	0.5	0.2	0.3
Th	0.2	0.4	0.7	0.3	0.3	0.3	0.3	0.4	0.4	0.3	0.9
U	0.2		0.6	0.1	0.2		0.1	0.2	0.5	0.1	0.4
Pb	2.1		0.8	0.3	0.7		0.6	1.5	1.1	0.4	1.9
Ba/Rb	13.4	56.7	10.3	18.5	21.3	0.0	16.4	12.4	63.2	3.4	5.0
La/Sm_n	0.8	0.8	0.8	0.6	0.5	0.6	0.6	0.6	0.7	0.7	0.6
Gd/Yb_n	1.4	1.2	1.2	1.0	1.1	1.1	1.1	1.0	1.0	1.1	1.1
La/Yb_n	0.9	0.7	1.0	0.6	0.5	0.6	0.7	0.6	0.7	0.7	0.6
$(Eu/Eu^*)_n$	1.1	1.1	1.0	0.8	0.8	0.9	0.8	0.8	0.8	1.0	0.9
Nb/La_{pm}	0.5	0.5	0.3	0.9	1.5	0.7	0.7	0.6	0.8	0.8	1.0
Th/La_{pm}	0.4	7.7	1.1	0.7	0.9	0.5	0.5	0.5	0.5	0.5	1.5
Nb/Th_{pm}	1.4	0.1	0.3	1.3	1.7	1.4	1.5	1.2	1.8	1.5	0.6
$(Ti/Ti)^*$	0.8	0.9	0.9	1.1	1.1	1.1	1.1	1.1	1.0	1.0	0.9
$(Zr/Zr)^*$	0.9	1.1	1.3	1.5	1.6	1.3	1.6	1.4	0.9	1.6	1.5
Zr/Hf	32.7	46	69.0	35.6	28.8	42.9	57.1	57.5	22.5	44.7	40.0
Zr/Nb	29.5	36.8	36.3	36.7	40.6	40.5	37.7	34.5	34.1	39.6	39.5
Nb/Ta	9.5	11.1	15.3	12.1	17.6	15.9	14.1	10.9	12.4	17.9	18.8
Al_2O_3/TiO_2	12.4	7.9	9.5	7.5	7.8	5.7	6.2	4.4	5.9	5.6	4.9
CaO/Al_2O_3	0.58	0.97	0.38	0.54	0.30	0.88	0.77	0.80	0.59	0.59	0.35

	12 Ch-28-09	13 97-116	14 97-117	15 97-118	16 97-119-3	17 C-29d-09	18 C-29b-09	19 C-26g-09	20 97-102	21 97-101
SiO_2	47.4	49.3	49.7	48.2	50.4	46.3	48.3	52.5	52.8	45.1
TiO_2	2.57	2.43	2.39	2.45	2.67	2.90	2.17	3.83	2.61	2.06
Al_2O_3	13.5	13.2	11.7	12.6	15.7	15.8	18.6	15.6	16.4	16.2
Fe_2O_3	14.3	15.0	14.8	15.2	9.9	12.3	11.0	13.6	12.1	13.1
MgO	6.53	6.70	7.33	6.66	2.54	4.83	4.59	2.63	2.28	5.95
CaO	10.21	6.80	8.90	9.09	9.36	10.16	7.50	3.62	4.55	9.56
MnO	0.20	0.21	0.20	0.19	0.17	0.20	0.14	0.17	0.20	0.18
Na_2O	3.02	3.05	2.51	2.05	3.33	3.75	3.22	3.52	4.60	2.23
K_2O	0.37	0.37	0.31	1.21	1.40	0.71	2.03	1.73	0.68	0.15
P_2O_5	0.23	0.25	0.21	0.22	0.36	0.34	0.27	0.70	0.84	0.41
L.O.I.	2.47	2.75	1.96	2.21	4.23	3.25	2.78	2.54	4.02	5.16
Total	100.9	100.0	100.0	100.1	100.0	100.6	100.6	100.4	101.0	100.0
Mg#	48	50	53	50	36	44	46	35	30	51
Rb	7.7	8.0	6.0	24.0	12.0	16.2	46.1	22.3	10.0	3.0
Sr	170	75	43	147	403	392	441	170	680	554
Y	57	47.2	44.4	48.8	43.7	25	19.0	39	39.1	20.2
Zr	183	131	127	132	218	190	152	306	238	132

Table 2 (continued)

	12 Ch-28-09	13 97-116	14 97-117	15 97-118	16 97-119-3	17 C-29d-09	18 C-29b-09	19 C-26g-09	20 97-102	21 97-101
Nb	4.0	3.5	3.2	2.7	8.7	19.3	15.4	43	35	16.6
Ba	42	200	200	200	259	88	226	370	368	184
La	4.7	5.2	4.5	5.7	13.8	12.7	10.3	29	32	21.5
Ce	14.6	18	13	18	35	29	23	61	70	45
Nd	14.3	17	15	17	27	18.3	14.6	39	41	24
Sm	4.7	6.3	5.6	6	8.2	4.8	3.8	9.1	10	5.7
Eu	1.6	1.9	1.5	1.9	2.6	1.6	1.3	3.4	3.1	1.7
Gd	7.1	8.6	7.7	8.3	9.3	4.9	4.1	9.9	10.1	5
Tb	1.2	1.4	1.4	1.5	1.6	0.8	0.6	1.3	1.6	0.8
Dy	8.0					4.3	3.3	6.8		
Ho	1.7					0.8	0.6	1.2		
Er	5.0					2.1	1.6	3.1		
Tm	0.8					0.3	0.2	0.4		
Yb	4.8	6.0	5.6	6	5.1	1.7	1.2	2.4	3.8	1.9
Lu	0.7	0.9	0.8	0.9	0.7	0.2	0.2	0.3	0.5	0.3
Hf	4.6	4.7	4.1	4.2	5.9	4.3	3.6	7.1	5.9	3.3
Ta	0.2	0.2	0.3	0.2	0.7	1.2	1.0	2.7	2.2	1.0
Th	0.8	0.5	0.5	0.4	0.8	1.3	1.0	3.4	2.8	2.1
U	0.2	0.3		0.1		0.9	0.5	1.0	1.5	0.8
Pb	0.7	1.5	2.0	0.5	3.0	1.4	0.7	6.4		
Ba/Rb	5.4	25.0	33.3	8.3	21.6	5.4	4.9	16.6	36.8	61.3
La/Sm$_n$	0.6	0.5	0.5	0.6	1.1	1.7	1.7	2.0	2.0	2.4
Gd/Yb$_n$	1.2	1.2	1.1	1.1	1.5	2.4	2.5	3.3	2.1	2.1
La/Yb$_n$	0.7	0.6	0.5	0.6	1.8	5.0	5.7	8.1	5.7	7.5
(Eu/Eu*)$_n$	0.9	0.8	0.7	0.8	0.9	1.0	1.0	1.1	0.9	1.0
Nb/La$_{pm}$	0.8	0.6	0.7	0.5	0.6	1.5	1.4	1.4	1.1	0.7
Th/La$_{pm}$	1.3	0.8	0.9	0.6	0.5	0.8	0.8	0.9	0.7	0.8
Nb/Th$_{pm}$	0.6	0.8	0.8	0.8	1.3	1.8	1.8	1.5	1.5	0.9
(Ti/Ti)*	0.9	0.8	0.9	0.8	0.8	1.5	1.3	1.0	0.6	0.9
(Zr/Zr)*	1.6	0.9	1.0	0.9	1.0	1.4	1.4	1.1	0.8	0.7
Zr/Hf	46.2	37.4	39.7	48.9	25.1	9.8	9.9	7.2	6.8	8.0
Zr/Nb	39.9	27.9	31.0	31.4	36.9	44.3	41.7	43.4	40.3	40.0
Nb/Ta	18.7	23.3	12.3	18.0	13.4	16.0	14.9	15.9	15.8	17.5
Al$_2$O$_3$/TiO$_2$	5.3	5.4	4.9	5.2	5.9	5.5	8.6	4.1	10.2	7.8
CaO/Al$_2$O$_3$	0.75	0.52	0.76	0.72	0.57	0.64	0.40	0.17	0.14	0.59

Columns: 1–5 – depleted basalts (MORB-type); 6–15 – transitional basalts (OPB-type); 16–21 – enriched basalts (OIB-type). The major oxides in 2, 13–15 and 20 were previously reported in Safonova et al. (2004) and the data for 16 and 21 are from Safonova et al. (2009).

Table 3
Average values of key major and trace elements and element ratios used for distinguishing three groups of basalts from the Char SSZ.

	Group 1 N = 5	Group 2 N = 10	Group 3 N = 6	N-MORB[a]	E-MORB	OIB
TiO$_2$, wt.%	1.66	2.47	2.54	1.27	1.00	2.87
MgO, wt.%	6.88	6.28	3.97			
P$_2$O$_5$, wt.%	0.14	0.24	0.49	0.11	0.14	0.62
Mg#	52	47	40			
Y, ppm	32	50	31	28	22	29
Zr, ppm	108	163	206	74	73	280
Ba, ppm	45	104	249	6.3	57	350
Nd, ppm	9.8	15.4	27.3	7.3	9	38.5
Sm, ppm	3.5	5.5	6.9	2.63	2.6	10
Hf, ppm	3.0	4.6	5.0	2.05	2.03	7.8
Th, ppm	0.4	0.5	1.9	0.12	0.6	4
La/Sm$_n$[b]	0.7	0.6	1.8	0.6	1.5	2.3
Gd/Yb$_n$[b]	1.3	1.1	2.3	1	1.3	2.9
La/Yb$_n$[b]	1.4	0.6	5.6	0.7	1.8	11.5
ΣREE, ppm	48.6	73.4	115.9	37.8	47	189
Zr/Nb	42.4	43.7	9.0	31.8	8.8	5.8
CaO/Al$_2$O$_3$	0.51	0.67	0.42	0.75	0.73	0.67

[a] The values for chondrite, N-MORB, E-MORB and OIB are from Sun and McDonough (1989).
[b] Ratios normalized to chondrite.

Nb/Y diagram (Winchester and Floyd, 1977), the samples of Groups 1 and 2 mostly plot in the field of subalkaline basalts, whereas those of Group 3 plot in the field of alkaline basalt and trachyandesite (Fig. 6B). In the Al$_2$O$_3$–TiO$_2$ + FeO–MgO triangle diagram (Jensen, 1976), subalkaline basalts of all three groups mostly plot in the field of high-Fe tholeiites (Fig. 6C).

5.1. Major elements

The three groups of basaltic samples are characterized by different but not widely variable concentrations of MgO, TiO$_2$ and P$_2$O$_5$ (Tables 2 and 3). The low-Ti and P and medium-Mg basalts of Group 1 (averages: TiO$_2$ = 1.64, MgO = 6.61, P$_2$O$_5$ = 0.18 wt.%), the high-Ti, medium-Mg and P basalts of Group 2 (averages: TiO$_2$ = 2.47, MgO = 6.28, P$_2$O$_5$ = 0.24 wt.%), and the high-Ti and P, low-Mg basalts of Group 3 (averages: TiO$_2$ = 2.54, MgO = 3.97, P$_2$O$_5$ = 0.49 wt.%; Table 3) coexist within this geological structure (Figs. 2 and 3). The basalts of Groups 1 and 2 are characterized by iron and titanium enrichment during fractionation (Fig. 7A) and plot along the tholeiitic trend suggesting similar conditions of crystallization (Fig. 7B). However, they show no clear trends in the MgO versus Al$_2$O$_3$/TiO$_2$ plot suggesting insignificant fractionation of Fe–Ti-oxides (Fig. 7C). Groups 1 and 2 basalts are compositionally similar to Western Pacific ridge basalts (MORB) except for the content of TiO$_2$ (Fig. 8A). According to the content of MgO the basalts of Groups 1 and 2 are medium magnesian with averages of 6.6 and 6.3 wt.%, respectively, compared to Group 3 basalts with an average of 3.9 wt.% (Table 2; Fig. 8A–D). The high TiO$_2$ contents and FeO*/MgO ratios (>1) in Group 3 basalts correspond to a higher degree of crystallizational differentiation. The contents of TiO$_2$ and P$_2$O$_5$ increase with decreasing MgO in Groups 1 and 2 (Fig. 8A and D).

The major element data cluster into three groups. Groups 1 and 3 correspond to MORB and OIB (illustrated by examples from the western Pacific and Hawaii in Fig. 8), respectively, whereas Group 2 appears to represent a transitional chemical group (Fig. 8A–D).
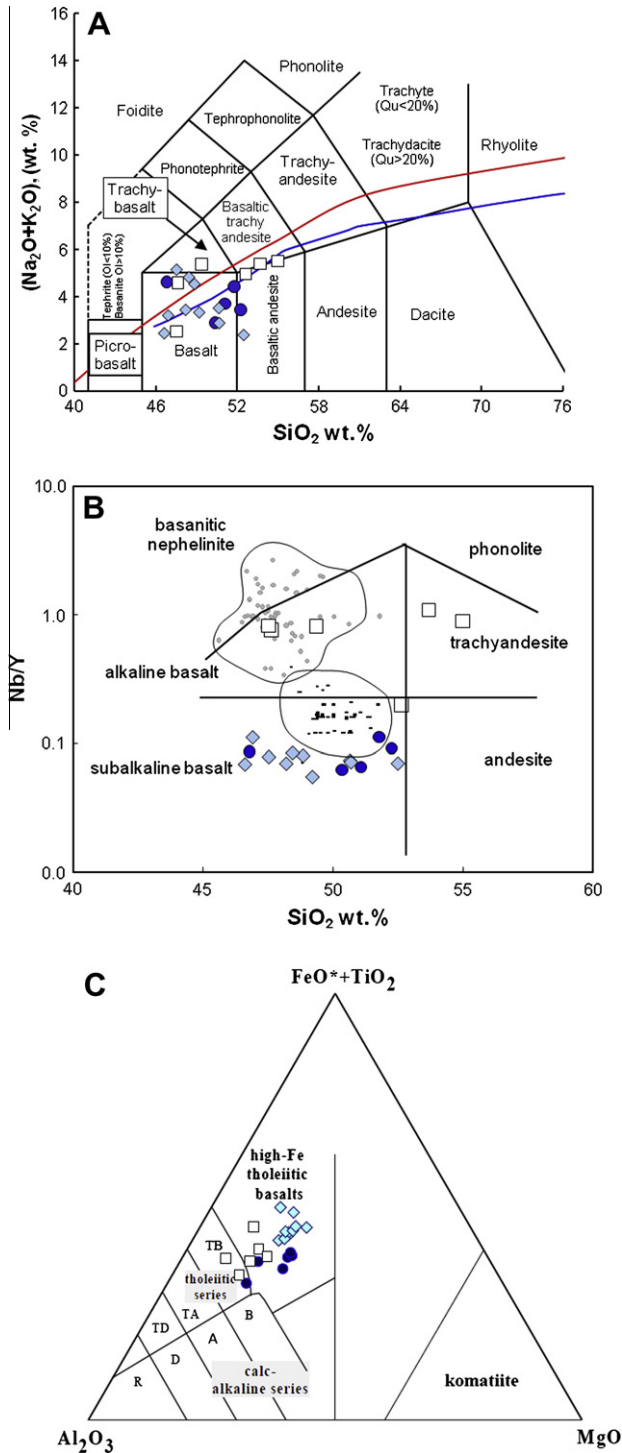
Fig. 6. Classification diagrams for Char basalts. (A) TAS (Le Maitre et al., 2002). (B) Nb/Y versus SiO_2 classification diagram (Winchester and Floyd, 1977). (C) Al_2O_3–FeO^*+TiO_2–MgO diagram (Jensen, 1976); tholeiitic series: TA – andesite, TD – dacite, TR – rhyolite; calc-alkaline series: CB – basalt, CA – andesite, CD – dacite, CR – rhyolite; kom – komatiite. Symbols: circles – Group 1 (depleted), rhombs – Group 2 (transitional), squares – Group 3 (enriched); small rectangles – Western Pacific mid-oceanic ridge basalts (MORB), small gray circles – Pacific hot-spot basalts (OIB). OIB and MORB are from the GEOROC database (http://georoc.mpch-mainz.gwdg.de/georoc).

This grouping is more evident in the MgO versus TiO_2 and P_2O_5 (Fig. 8A and D), and MgO versus Al_2O_3/TiO_2 (Fig. 7C) plots. Groups 1 and 2 samples have MORB-like CaO/Al_2O_3 of 0.51 and 0.67 (in average), respectively, whereas Group 3 basalts have CaO/Al_2O_3 of 0.42 (Table 2).
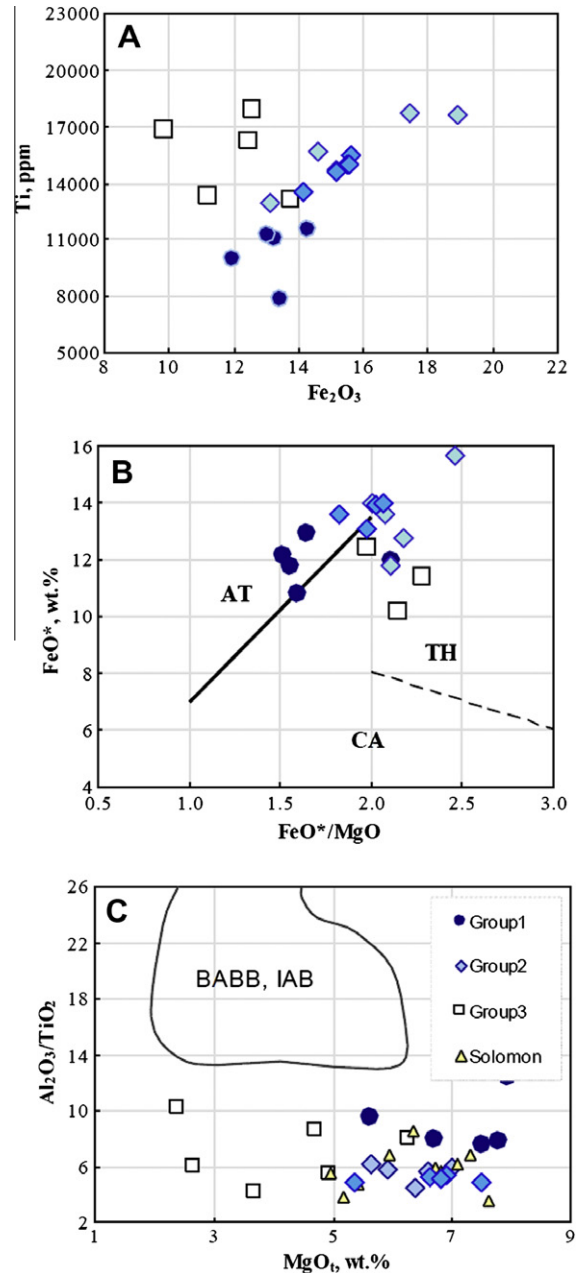
Fig. 7. Bivariant plots FeO^* versus FeO^*/MgO (A); TiO_2 versus FeO^*/MgO (B); MgO versus Al_2O_3/TiO_2 (C). Discriminant fields for abyssal tholeiite (AT), tholeiite (TH) and calc-alkaline volcanic rocks (CA) are after (Miyashiro, 1973); the data for back-arc basin basalts (BABB) and island-arc basalts (IAB) are from GEOROC database (http://georoc.mpch-mainz.gwdg.de/georoc) and data for the Solomon volcanic rocks are from Tejada et al. (1996).

Some of the major element variation undoubtedly is the result of alteration (see Section 6.1). These effects, however, are minimized in diagrams using FeO (or Fe_2O_3), Al_2O_3 and TiO_2 (Figs. 7 and 8A–C), where the distinct groupings of data are likely to reflect variations in primary magma composition or degree of differentiation.

5.2. Trace elements

The three groups defined by major elements also are distinguished by their trace element signatures (Table 3; Fig. 8). The MORB-type basalts (Group 1) have the lowest concentrations of La, Nb, and Zr (Fig. 8E–G). The transitional varieties (Group 2) have
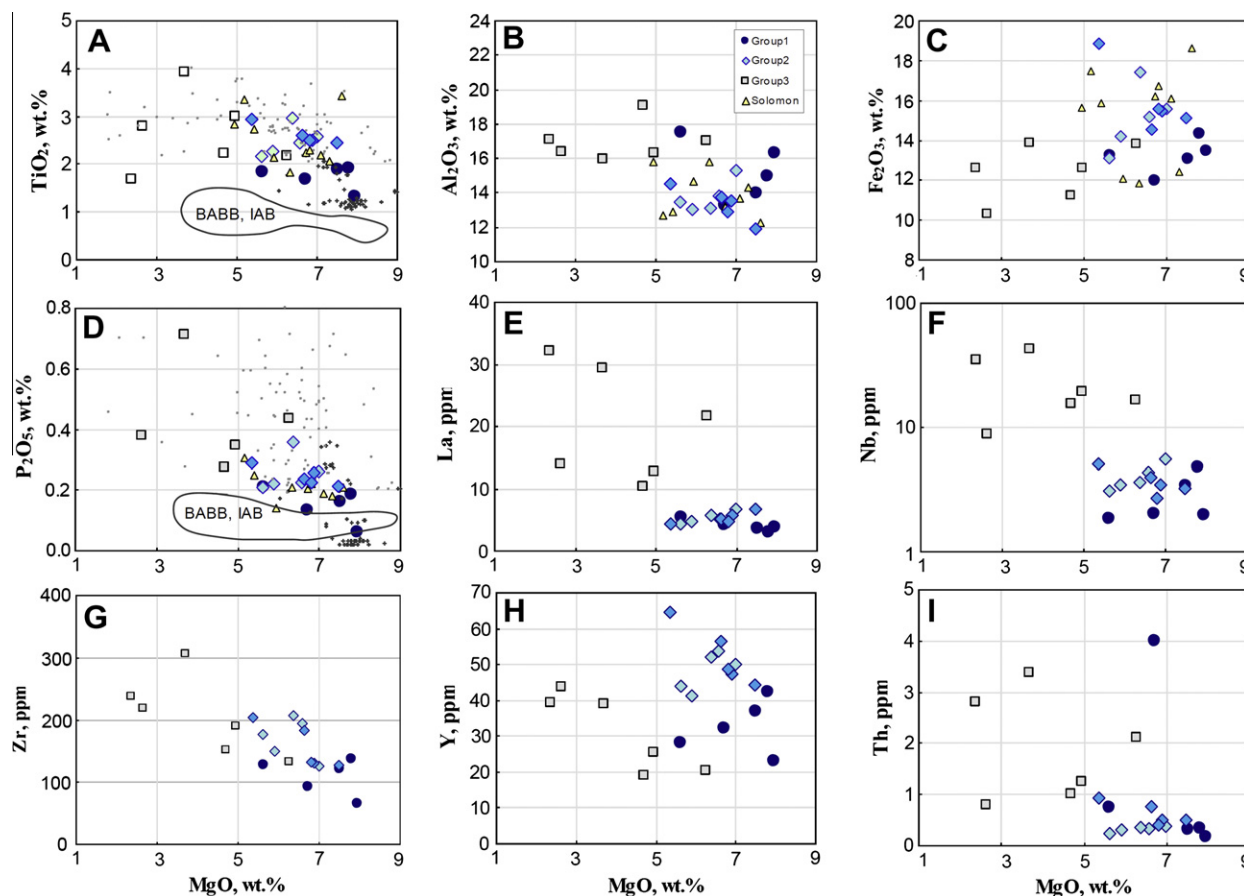
Fig. 8. Major and trace element data versus MgO (wt.%) for oceanic basalts from the Char SSZ. The data for the Solomon arc are from Tejada et al. (1996). Small symbols: gray dots – OIB-type basalts of the Hawaii chain of volcanoes; crosses – MORB-type basalts of the East Pacific Rise (GEOROC).

intermediate Nb, and Zr, but the highest Y contents (Fig. 8F–H). The OIB-type volcanics (Group 3) are enriched in typical "plume-related" incompatible elements, such as La, Nb and Th (Fig. 8E, F, and I).

In *Group 1* the concentrations of Zr and Y increase with decreasing MgO and those of La Nb, and Th all fall in narrow intervals (Fig. 8E, F, and I). The Zr/Nb ratios range from 32.7 to 69 (42.4 in average; Tables 2 and 3). This group of MORB-type volcanic rocks contain the lowest amounts of TiO_2, P_2O_5, Nb, Zr, La, Sm, and Th (Fig. 8) and possess flat REE patterns (Fig. 9A; La_{Nav} = 10; La/Yb_N = 0.54–0.97) showing little depletion in LREE and weak HREE differentiation (La/Sm_N = 0.5–0.8; Gd/Yb_N = 1.0–1.4). Two samples display small negative Eu anomalies (Eu/Eu* = 0.8). In the multi-element spectra (Fig. 9D) Nb is depleted relative to La (Nb/La_{pm} = 0.5–0.9) and both depleted and enriched in several samples relative to Th (Nb/Th_{pm} = 0.1–1.7). Values of Nb/La_{pm} < 1 are typical for many MORB rocks (Haase, 2002), but those of Nb/Th_{pm} < 1 are not. As Th in some samples seems to be enriched relative to other samples of Group 1 basalts, late- and post-magmatic alteration cannot be ruled out. Thus, ratios involving Th are not used as geochemical source indicators (see also Section 6.1). Three samples are characterized by positive Zr–Hf anomalies (Zr/Zr* = 1.3–1.6; Hf/Hf* = 1.2–1.4; Table 2; Fig. 9D).

Group 2 is special for a combination of trace element features: compared to Group 1 (MORB-type) the basalts are characterized by similar Nb, La, Th, but notably higher Ti, Sm, Zr, and Y (Table 3; Fig. 8E–I). Concentrations of Zr increase as MgO contents decrease (Fig. 8G). In Group 2 basalts, Al_2O_3, P_2O_5, La, Th, and Nb do not vary with MgO contents (Fig. 8). Ratios of Zr/Nb vary from 37.4 to 57.5 with an average of 43.7, i.e., similar to that in Group 1 with an average of 42.2 (Table 2). The flat REE patterns with slightly depleted LREE (Fig. 9B) and the mean values of La_N (10.8), La/Yb_N (0.6), La/Sm_N (0.6) and Gd/Yb_N (1.1) are close to those in Group 1 (Table 3). Group 2 rocks, however, have higher total REE contents than Group 1 rocks. Small Eu negative anomalies are observed in several samples (Eu/Eu* = 0.7–0.9). In the multi-element spectra of Group 2 (Fig. 9E) Nb is also depleted relative to La (Nb/La_{pm} = 0.46–1.0) and Th may be both depleted and enriched relative to Nb (Nb/Th_{pm} = 0.63–1.76). Interestingly, Group 2 basalts represent a geochemically transitional group of volcanic rocks, which according to most major and trace element data is similar to the high-Ti Sigana basalts and San Jorge volcanics of Malaita and Santa Isabel of the Solomon Islands (Tejada et al., 1996) (Figs. 8 and 9B and E).

Group 3 basalts have compositions clearly different from those of Groups 1 and 2 showing enrichment in incompatible elements such as Ti, Nb, Th, and LREE in MgO versus trace elements plots (Fig. 8). The increase of Y, Nb, Zr, and Sm with decreasing MgO contents is also typical of Group 3 basalts. The Zr/Nb ratios are lower than those in Groups 1 and 2, and range from 6.8 to 9.8, except for one sample with 25.1 (nine in average; Tables 2 and 3). Compared to Groups 1 and 2, the chondrite-normalized REE patterns of Group 3 basalts display enrichment in LREE: La_{Nav} = 54.3; La/Yb_{Nav} = 5.6 (Fig. 9C). No Eu anomalies are observed. The degree of LREE and HREE differentiation is medium: La/Sm_N varies from 1.1 to 2.4, and Gd/Yb_N – from 1.5 to 3.3. The PM normalized multi-element spectra (Fig. 9F) show that most of the samples with highly differentiated REE possess positive Nb anomalies relative to La and Th (Nb/La_{pm} = 0.6–1.47; Nb/Th_{pm} = 0.94–1.84), which is a diagnostic feature of plume-related oceanic island basalts (OIB-type). There
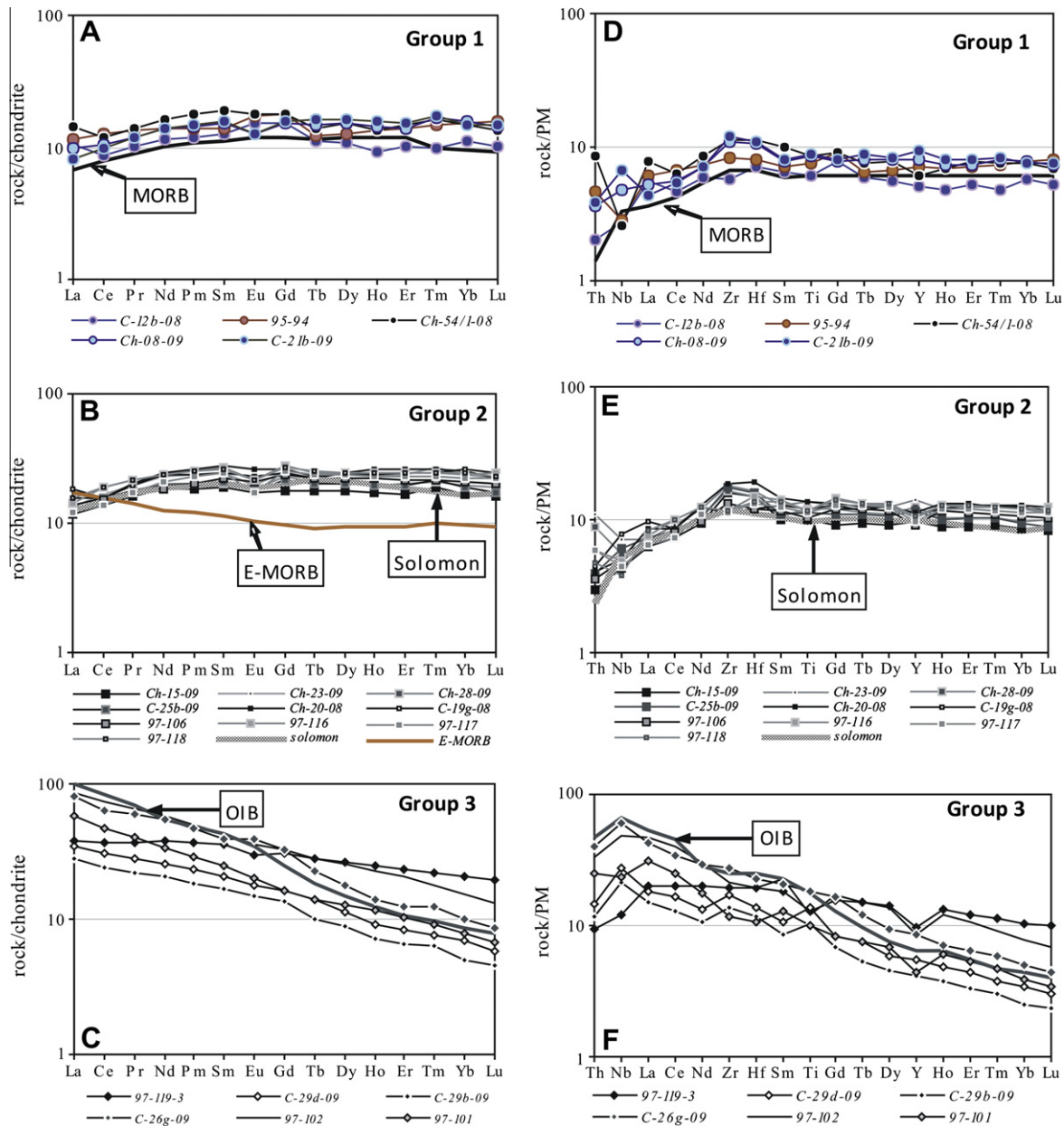
Fig. 9. Chondrite-normalized rare-earth element and primitive mantle-normalized multi-component trace element patterns for oceanic basalts from the Char SSZ. OIB, MORB and normalization values are from Sun and McDonough (1989). The data for the Solomon arc are from Tejada et al. (1996).

are highly (97-102, C-26g-09; Char site in Fig. 2) and less (C-29d-09, C-29b-09; Nikolaevka site in Figs. 2 and 3) incompatible element enriched subgroups in Group 3 basalts (Fig. 9C and F; Table 2). The geochemical features of Group 3 basalts are consistent with their formation from a plume-related mantle source, enriched in incompatible elements, especially in HFSE and LREE.

Thus, these three groups of basalts are distinguished based on variable concentrations of major elements (TiO, MgO, P_2O_5), HFSE (Y, Zr, Hf), MREE (Sm, Nd), Zr/Nb, total REE and/or La/Yb_N (Table 3), suggesting different types of mantle sources and different conditions of petrogenesis, first of all, degrees of melting and fractional crystallization.

5.3. Isotopes

The Sr, Nd, and Pb isotope data for basalts of the Char suture-shear zone are shown in Table 4 and Fig. 10. The compositional range of the data reflects the variable effects of (i) initial isotopic contrasts reflecting different sources, (ii) effects of alteration of the rocks by sea-water, and (iii) possible fractionation between the parent and daughter isotopes during later low-grade metamorphism, which may have affected in particular secondary minerals that formed during interaction of the rocks with sea water. Such late changes in the parent-to-daughter element ratios, which result in over- and under-correction of the *in situ* radiogenic growth of the daughter isotope, in particularly affect the Rb–Sr and the U–Th–Pb systems, as the parent and daughter elements of these systems behave geochemically different. The selective dissolution of secondary minerals during the leaching of samples may result in the preferential removal of the parent or daughter element, depending on (i) the distribution of these elements between "fresh" rock and selectively dissolved secondary minerals, (ii) the relative portion of the secondary minerals in the bulk sample, and (iii) the time difference between formation of the rocks and

Table 4
Whole-rock Sr, Nd, and Pb isotope data of Late Devonian–Early Carboniferous basalts from the Char suture-shear zone, East Kazakhstan.

Sample	$^{87}Sr/^{86}Sr$[a]	$^{87}Sr/^{86}Sr_{(T)}$[b]	$^{143}Nd/^{144}Nd$[a]	$\varepsilon Nd_{(T)}$[b]	$^{206}Pb/^{204}Pb$[c]	$^{207}Pb/^{204}Pb$[c]	$^{208}Pb/^{204}Pb$[c]	$^{206}Pb/^{204}Pb$[d]	$^{207}Pb/^{204}Pb$[d]	$^{207}Pb/^{204}Pb$[d]
C-12b-08	0.705485 ± 4	0.70534	0.512917 ± 5	4.6	17.985	15.545	37.708	17.63	15.53	37.61
Ch-54/1-08	0.707620 ± 4	0.70620	0.513002 ± 8	5.6	18.572	15.535	38.511	*15.86*	*15.39*	*37.31*
Ch-08-09	0.704702 ± 4	0.70440	0.513083 ± 6	7.8	18.530	15.468	38.264	*16.95*	*15.38*	*36.83*
C-21b-09	0.705352 ± 3	0.70504	0.513073 ± 9	7.4	20.079	15.545	37.786	19.25	15.50	*37.16*
Ch-15-09	0.705083 ± 3	0.70492	0.513048 ± 6	7.6	18.232	15.493	37.891	*17.17*	*15.43*	*37.38*
Ch-20-08	0.705773 ± 3	0.70526	0.513115 ± 9	8.1	17.980	15.466	37.652	17.41	15.44	37.36
C-19g-08	0.705322 ± 5	0.70516	0.513029 ± 5	7.1	19.689	15.618	37.907	18.87	15.57	37.64
Ch-23-09	0.711814 ± 4	0.70303	0.513143 ± 5	9.3	18.341	15.513	37.858	17.41	15.46	37.26
Ch-25b-09	0.709778 ± 8	0.70297	0.513173 ± 4	9.8	18.096	15.423	37.671	*16.90*	*15.36*	*36.73*
Ch-28-09	0.705713 ± 5	0.70506	0.513103 ± 9	9.0	18.104	15.493	37.909	*16.72*	*15.42*	*36.57*
Ch-29d-09	0.704430 ± 5	0.70383	0.512815 ± 5	5.2	20.255	15.612	38.761	17.66	15.47	38.64
Ch-29b-09	0.704803 ± 3	0.70330	0.512772 ± 9	4.5	19.890	15.580	39.136	*17.15*	*15.43*	37.27
Ch-26g-09	0.707400 ± 3	0.70553	0.512679 ± 9	3.5	18.620	15.560	38.695	18.03	15.53	38.03

[a] Sr and Nd were analyzed using dynamic multi-collection on a Triton and a Finnigan MAT262 multi-collector mass-spectrometer, respectively. Analytical uncertainties are given at $2\sigma m$ level. Reference materials NBS 987 and LaJolla gave $^{87}Sr/^{86}Sr$ = 0.701249 ± 5 (2σ, n = 20) and $^{143}Nd/^{144}Nd$ = 0.511846 ± 8 (2σ, n = 6), respectively.

[b] $^{87}Sr/^{86}Sr_{(T)}$ and $\varepsilon Nd_{(T)}$ were calculated for 350 Ma using $\lambda^{87}Rb$ = 1.42E−11 y^{-1} and $\lambda^{147}Sm$ = 6.54E−12 y^{-1}, $(^{147}Sm/^{144}Nd)^0_{CHUR}$ = 0.1967, and $(^{143}Nd/^{144}Nd)^0_{CHUR}$ = 0.512638, respectively, and the concentration data given in Table 2 (the data for CHUR are from Jacobsen and Wasserburg (1984)).

[c] Pb was analyzed on a Finnigan MAT262 multi-collector mass-spectrometer using static multi-collection. Lead isotope data corrected for mass discrimination with 0.1%/A.M.U. Reproducibility at 2σ level is better than 0.1%.

[d] Lead isotope data recalculated to 350 Ma using the contents of Pb, U and Th (Table 2) and the constants recommended by IUGS ($\lambda^{232}Th$ = 4.9475E−11 y^{-1}, $\lambda^{235}U$ = 9.8485E−10 y^{-1}, and $\lambda^{238}U$ = 1.55125E−10 y^{-1}). Numbers in italics refer to obvious poly-stage systems that seem to have been affected by Pb and/or U mobility. For discussion see text.

the formation of the secondary minerals. To avoid artefacts originating from the correction of *in situ* radiogenic growth, only the measured Pb isotope data are shown in Fig. 10. In contrast, as *in situ* ^{87}Sr growth is small for most samples, Fig. 10 shows the $^{87}Sr/^{86}Sr$ values recalculated to 350 Ma. Recalculation of the isotopic data to 320 Ma or 380 Ma, i.e., the minimum and the maximum age of the basalts yields slightly higher and lower $^{87}Sr/^{86}Sr$ values, respectively, than shown in Table 4, but does not change the data pattern as shown in Fig. 10A. Therefore, only the recalculations to 350 Ma are shown.

All samples have positive εNd_{350} values and relatively high initial $^{87}Sr/^{86}Sr$ ratios. They fall to the right of the mantle array (for 350 Ma), which is due to addition of more radiogenic Sr from the seawater. The εNd_{350} values range from +3.5 to +9.8 (Table 4). The Nd isotopic compositions of rocks of Group 1 and Group 2 overlap, ranging from 4.6 to 7.8 and from 7.1 to 9.8, respectively, although there is a tendency of Group 2 rocks to have higher εNd_{350} values. Basalts of Group 3 have generally lower values than the other two groups ranging from 3.5 to 5.2 (Fig. 10A).

The Pb-isotope data encompass a broad range from relatively unradiogenic compositions with $^{206}Pb/^{204}Pb \sim 18$ to relatively radiogenic Pb with $^{206}Pb/^{204}Pb > 20.5$ (Table 4). *In situ* Pb growth over the last 350 Ma has shifted the Pb isotopic composition to more radiogenic compositions. In the $^{206}Pb/^{204}Pb$ versus $^{207}Pb/^{204}Pb$ diagram, the deviation of the data from the 350 Ma reference line (Fig. 10C) demonstrates contrasting initial Pb isotopic composition among samples of each basalt group. This heterogeneity could either reflect isotopic heterogeneity of the mantle source of the various basalts, assimilation of old crustal material, or lead addition during interaction of the basalts with seawater. In the $^{206}Pb/^{204}Pb$ versus $^{208}Pb/^{204}Pb$ diagram, most samples plot along the Pb growth lines for mantle and upper crustal rocks (Fig. 10B). The four samples that fall off these growth curves to higher $^{206}Pb/^{204}Pb$ values have experienced distinct U addition that resulted in the preferential growth of uranogenic Pb. Note, such a U addition will not become apparent in the $^{206}Pb/^{204}Pb$ versus $^{207}Pb/^{204}Pb$ diagram unless for accelerated Pb growth. As U generally is soluble in aqueous fluids, U may uncouple from Th by fluid-mediated processes, as for instance during interaction of the basalts with seawater or the modification of the mantle wedge by fluid derived from the subducting slab.

6. Discussion

6.1. Geochemical signatures of secondary alteration and crustal contamination

Evidence for secondary alteration of all Char basaltic samples comes from variably high LOI (1.9–4.8%). Generally, it is more difficult to identify the origin of Paleozoic mafic volcanic rocks than their Mesozoic and Cenozoic analogues. This, first of all, is because Na, K and the low-field strength elements (i.e., LILE) are relatively mobile and susceptible to change during underwater basalt eruption over the oceanic floor due to water–rock interaction and during other processes of post-magmatic alteration compared to HFSE (e.g., Humphris and Thompston, 1978; Thompson, 1991). In our case, evidence for the mobility of the LILE comes from the wide variations of their concentrations (Table 2). For example, Ba/Rb ratios range from 10.3 to 56.7 in Group 1 (Sr = 68–120, Rb = 1–76, Ba = 13–78), from 3.4 to 63.2 in Group 2 (Sr = 30–147, Rb = 0.9–3.7, Ba = 24–200) and from 4.9 to 61.3 in Group 3 (Sr = 170–680, Rb = 3–46, Ba = 88–368). Therefore, we excluded most LILE from the multi-element diagrams (Fig. 9B, D, and E) and base our interpretation on the relatively immobile incompatible elements, in particular, the REE, Nb, Zr, Hf, and Y, which are less prone to alteration (e.g., Floyd and Winchester, 1975; Polat et al., 1999).

The wide variations in the isotopic composition of Sr and Pb (see Section 5.3), namely the increased $^{87}Sr/^{86}Sr$ and $^{206}Pb/^{204}Pb$ ratios (Fig. 10) also are in line with water–rock interaction for most Char basalts, with addition of relatively radiogenic Sr and the increase of Rb/Sr and U/Pb.

Three samples appeared too enriched in Th relative to Nb resulting in Th/Nb$_{pm}$ > Th/La$_{pm}$ (Fig. 9). Valsami-Jones and Ragnarsdottir (1997) found that Th, also a HFSE, can be mobile during high temperature water–rock interaction, which takes place during submarine eruption of basaltic lavas. The mobility of Th was previously suggested for a number of samples of Early Paleozoic oceanic basalts hosted by the Kurai, Katun and Zasur'ya accretionary complexes in Russian Altai, western CAOB (Nos. 3 and 4 in Fig. 1; Safonova et al., 2008, 2011a, 2011b). Therefore, in the following discussion of basalt origin and geodynamic settings we will use mainly the HFSE (Th with caution) and REE to identify the magmatic affinity and petrogenesis of these altered mafic volcanic rocks.
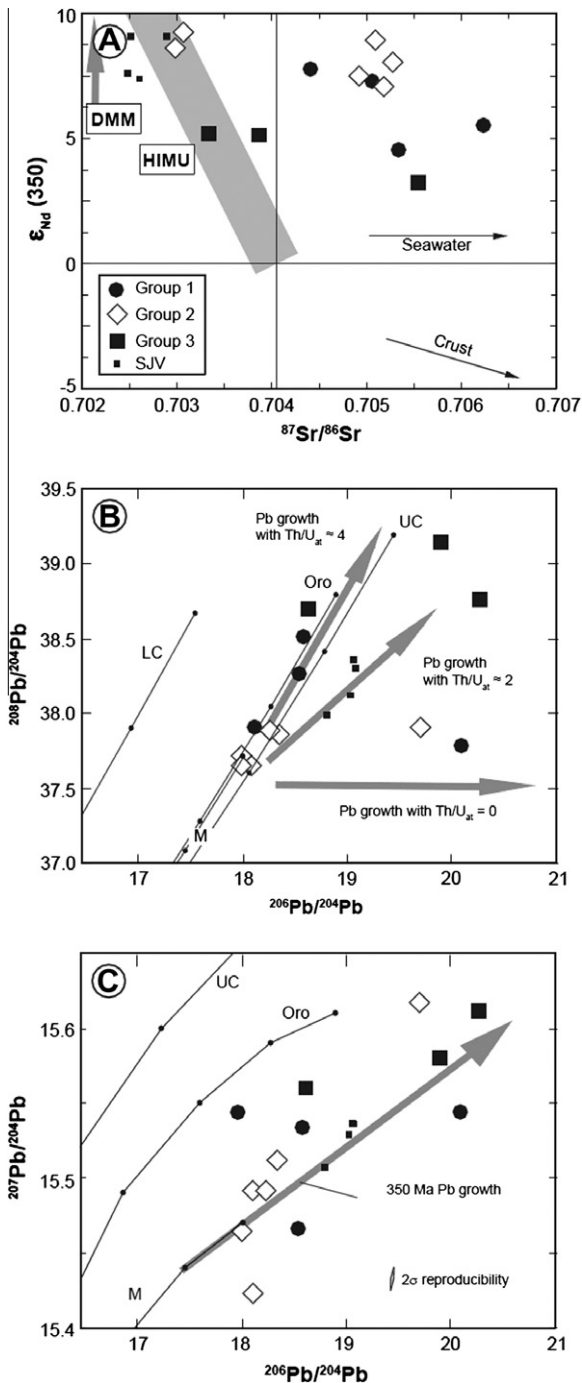
Fig. 10. Isotopic composition of basalts of the Char Zone. (A) $^{87}Sr/^{86}Sr$ versus εNd_{350} isotope data for basalts of the Char Zone, recalculated to 350 Ma. Note that most samples fall to the right of the mantle array, indicating exchange of Sr between basalts and seawater. (B and C) Measured Pb isotope data together with the lead growth curves of Zartman and Doe (1981). M = mantle; LC = lower crust; UC = upper crust; Oro = Orogenic Pb; DMM = depleted mantle; SJV = San Jorge volcanics of the Solomon arc; ticks at 400 Ma intervals. Gray arrow in the $^{206}Pb/^{204}Pb$ versus $^{207}Pb/^{204}Pb$ diagram shows how the initial Pb isotopic composition of the basalts is shifted by *in situ* Pb growth. Addition of old crustal lead would displace the Pb isotopic compositions towards the UC and Oro growth curves. In the $^{206}Pb/^{204}Pb$ versus $^{208}Pb/^{204}Pb$ diagram, the gray arrows indicate how the Pb isotopic composition changes with time for different Th/U_{at} (at = atomic) ratios. The addition of U during seawater alteration would shift Th/U_{at} to lower values and with time result in Pb isotopic compositions that fall markedly to the right of the average Pb growth curves. Similarly, modification of the mantle by subducted sediments may reduce Th/U_{at} and, thus, eventually result in Pb falling to the right of the Pb growth curves.

However, some of the anomalous geochemical signatures (e.g., Th enrichment, Nb depletion) cannot be fully explained by water–rock interaction during eruption and post-magmatic alteration of the lavas, but may reflect the effect of crustal contamination (this section) and variable degree of fractional crystallization and melting (see Sections 6.2 and 6.3).

Contamination by continental crust is quite possible, however, several lines of geological evidence favor an intra-oceanic setting for the formation of the basalt sequences (Polyanskii et al., 1979; Ermolov et al., 1981; Iwata et al., 1997; Buslov et al., 2001; Dobretsov, 2003; Safonova et al., 2004, 2009). The presence of multi-colored chert with radiolarians and conodonts, in places having direct contacts with tholeiitic basalts (Fig. 4B), suggests a marine environment rather than a continental/active margin setting for the eruption of these volcanic rocks. As far as the continental crust is characterized by Nb minimums in PM-normalized multi-component diagrams (Sun and McDonough, 1989), most crustally contaminated lavas are characterized by both $Th/Nb_{pm} > 1$ and $La/Nb_{pm} > 1$ (e.g., Redman and Keays, 1985; Arndt and Jenner, 1986). Island-arc/suprasubduction basalts and even back-arc basin tholeiites are characterized by $Th/Nb_{pm} > La/Nb_{pm}$, it being known that Th/Nb_{pm} usually exceeds 2.0 (GEOROC database; Safonova et al., 2009). Several multi-element spectra of Groups 1 and 2 basalts show the enrichment of Th in respect to Nb (Fig. 9B and E), however, (i) Nb/La_{pm} do not correlate with Th/La_{pm}; (ii) $Th/La_{pm} < 1$ in most samples; (iii) the concentrations of Th are rather low: 0.39 and 0.47 in average for Groups 1 and 2, respectively, compared to the averages of 1.4 for the Aleutian arc, 2.6 for the Honshu arc and 6.1 for the Ryukyu arc (Li et al., 2002; GEOROC database; Table 2). The higher Th contents and low Nb/Th_{pm} in three samples of tholeiitic basalts of Group 1 (Ch-54/1-08) and Group 2 (Ch-23-09, Ch-28-09; Table 2) may reflect secondary alteration, as Th/La_{pm} consistently is less than 2 (see above).

6.2. Fractional crystallization

Fractional crystallization may be proposed due to the medium to high variation of MgO within each group of basalts (Figs. 7 and 8) and the presence of phenocrysts of plagioclase and opaque minerals (Section 3; Fig. 5). The major and trace element geochemical features and geochemical modeling of fractionation indicate that (i) fractionation of clinopyroxene and, to a lesser degree, plagioclase affected the composition of basaltic lavas, (ii) fractionation of Ti–Fe oxides was not a important factor, and (iii) fractionation of clinopyroxene was essential.

The Eu anomalies in the REE spectra of some samples of Groups 1 and 2 suggest insignificant fractionation of plagioclase or post-magmatic alteration (Fig. 9B and E). Fractional crystallization control on the Nb negative anomalies in the basalts of Groups 1 and 2 (Fig. 9D and E) is quite probable because Nb is compatible in Fe-Ti oxides, which are likely to be fractionating phases. However, these samples display negative correlation between MgO and TiO_2 (Fig. 8A), their multi-element patterns show no notable Ti negative anomalies (Fig. 9D and E) and the Nb/La_{pm} ratios do not correlate with Mg# (Fig. 11A). Moreover, there is no correlation between concentrations of Nb/La_{pm} and TiO_2 (Fig. 11B). The modeled fractionation of clinopyroxene in the Nb–Zr system showed that it cannot explain the wide variation of Zr/Nb: the Nb trend is almost parallel to the Zr/Nb axis, whereas the pyroxene fractionation trend is perpendicular to it (Fig. 11C). Therefore we do not consider fractionation of Fe–Ti oxides or clinopyroxene as a factor of the redistribution of Nb after the formation of an initial basaltic melt.

No basalt group shows correlation between Fe_2O_3 and Nb/La_{pm} and Th/La_{pm} ratios. In addition, the narrow variation of La/Sm_n ratios in Group 1 (MORB-type) and Group 2 (transitional) basalts over a relatively wide range of Mg# (from 35 to 55; Table 2)
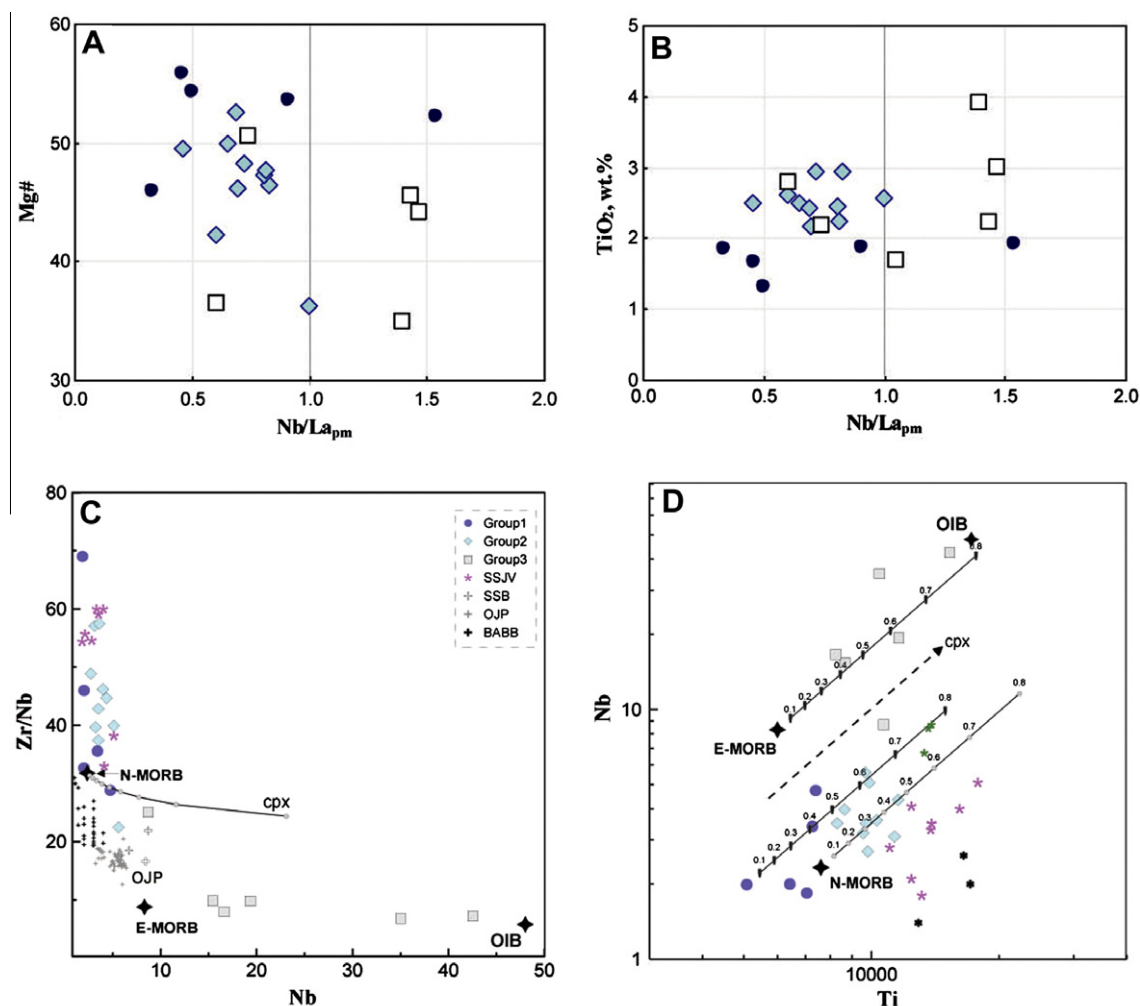
Fig. 11. Diagrams illustrating fractional crystallization: (A) Nb/La$_{pm}$ versus #Mg, (B) Nb/La$_{pm}$ versus TiO$_2$ and (C) Nb versus Zr/Nb, indicating no notable fractionation of Nb by Fe–Ti oxides (A and B) and clinopyroxene (C and D) Ti versus Nb plot showing lines of clinopyroxene fractionation of E-MORB, N-MORB and depleted MORB-type basalt (C-12b-08; Table 2) sources, which affected Ti concentrations. For discussion see text (Section 6.3). The data for the Solomon arc are from Tejada et al. (1996). Abbreviations: SSJV – Solomon San Jorge Volcanics, SSB – Solomon Sigana Basalts, OJP – Ontong-Java Plateau, BABB – back-arc basin basalts. Data for OIB, E-MORB and MORB are from Sun and McDonough (1989), for BABB – from GEOROC.

suggests that the fractional crystallization of clinopyroxene was not responsible for LREE fractionation. Consequently, we consider the Th–Nb–LREE inter-element ratios in the volcanic rocks to be rather independent of clinopyroxene or Fe–Ti oxide fractional crystallization (Fowler and Jensen, 1989; Polat et al., 1999).

The absence of clinopyroxene phenocrysts and the clear positive correlations between MgO and Al$_2$O$_3$ (Fig. 8B) do not allow us to fully exclude clinopyroxene fractionation from the parental magma. To understand the formation of the high-Ti basalts of Group 2, which are nevertheless depleted in other HSFE and LREE, we checked the fractionation of pyroxene as a probable factor controlling the content of Ti. Fig. 11D shows no notable fractionation of clinopyroxene in Group 1 basalts. On the other hand, the observed variations of Ti concentrations in most samples of Group 2 can be achieved by fractionation of 10–30% of pyroxene. For the calculations we used a Nb-depleted MORB-type melt and a hypothetical melt compositionally similar to the most Ti–Nb-depleted sample of Group 2, i.e., C-12b-09 (Table 2). Such fractionation could be possible in a shallower magma chamber. It is widely thought that shallow magma chambers are rare under thin oceanic lithosphere of mid-oceanic ridges (especially those with high rates of spreading, like in the modern Pacific), but rather common under thicker lithosphere, i.e., in intraplate (oceanic plateau)

or suprasubduction settings. Taking into account the geochemical characteristics of Group 2 basalts, showing no similarity with typical OIB and arc lavas (Figs. 8 and 9), we suggest that pyroxene fractionation resulting in increased Ti contents could take place in an intermediate chamber, whose formation was provoked by the deceleration of subduction by an accreting/subducting oceanic plateau.

The Ti-trend for the OIB-type basalts also could be obtained by clinopyroxene fractionation from an enriched, E-MORB type melt (Fig. 11D), however that would require much higher degrees of fractionation (40–80%), which is unrealistic. Therefore, we disregard crystallization of pyroxene as a factor responsible for the variation of TiO$_2$ in the Char OIB-type basalts. We rather believe that it was controlled by a heterogeneous character of their mantle source (see Sections 6.3 and 6.4).

6.3. Degrees of melting

Several samples of MORB-type and transitional basalts of Groups 1 and 2, respectively, display Nb depletions relative to Th and their absolute abundances of Nb are close to those in island-arc (Mariana, Aleutian), N-MORB and Ontong-Java plateau (OJP) basalts (Figs. 9B, E, and 12A). The Th enrichment relative to Nb

cannot be fully explained by secondary alteration or crustal contamination (Section 6.1), which could provide Th input, therefore we can check their suprasubduction versus oceanic origin via melting modeling. This is also important because oceanic basalts are sometimes erroneously regarded as island-arc basalts (Safonova, 2009) and a possible criterion for their discrimination could be a type of mantle source and the degree of melting in it, which control relationships between Th, Nb and HREE.

Pfander et al. (2002) used the Nb–Yb systematics to calculate the composition of melts produced by different degrees of melting and variable source compositions for the Late Neoproterozoic mafic rocks of the Agardagh opitolite, applying the equation for non-modal batch melting (Albarède, 1995). Similarly to the HFSE, the authors regarded the HREE as conservative elements, for which the contribution from the slab to the mantle wedge is minimal (Pearce and Peate, 1995). Following their approach, we tested the melting of primitive (garnet peridotite, spinel lherzolite) and moderately and high-Nb-depleted (depleted harzburgites) mantle sources, which could probably produce the basaltic melts (Pfander et al., 2002 and references therein; Parkinson and Pearce, 1998; Fig. 12A). Starting concentrations of Nb and Yb are taken as 0.71 and 0.49 ppm (Nb/Yb = 1.45) in the primitive mantle source (Sun and McDonough, 1989) and as 0.35 and 0.45 ppm (Nb/Yb = 0.78)

and 0.20 and 0.45 ppm (Nb/Yb = 0.44) in moderately and highly depleted mantle sources. The primitive values correspond to those in the N-MORB calculated for 10% batch melting of depleted mantle peridotite by (Hofmann, 1988). As Nb is less compatible than Yb, the Nb/Yb of the highly depleted mantle source was chosen to be less than that in the basalts, which lowest is 0.5 (Table 2; sample Ch-54-08).

Mantle source characteristics are shown in Table 5. Initial garnet abundances in the garnet peridotite were taken as 10%, 5% and 1%. Fig. 12A shows that the basalts of Groups 1 and 2, together with San Jorge basalts and Koloseru gabbro from the Solomon arc, plot near the melting lines of the two variably depleted harzburgites. Therefore, the basalts of Groups 1 and 2 could be produced at relatively high degrees of melting (5–15%) of a depleted mantle source. Group 2 basalts formed at slightly lower degrees of melting compared to Group 1 and Ontong-Java basalts (OJB), respectively. The OIB-type basalts of Group 3 formed at even lower degrees of partial melting (1–5%) of a source containing both spinel and garnet lherzolite (Fig. 12A).

To test our estimations of the degrees of melting in the Nb–Yb systematics, we performed similar calculations in the La/Sm–Lu/Hf system, which apart from HREE (Lu) and HFSE (Hf) also includes a representative of LREE and MREE. The La/Sm versus Lu/Hf
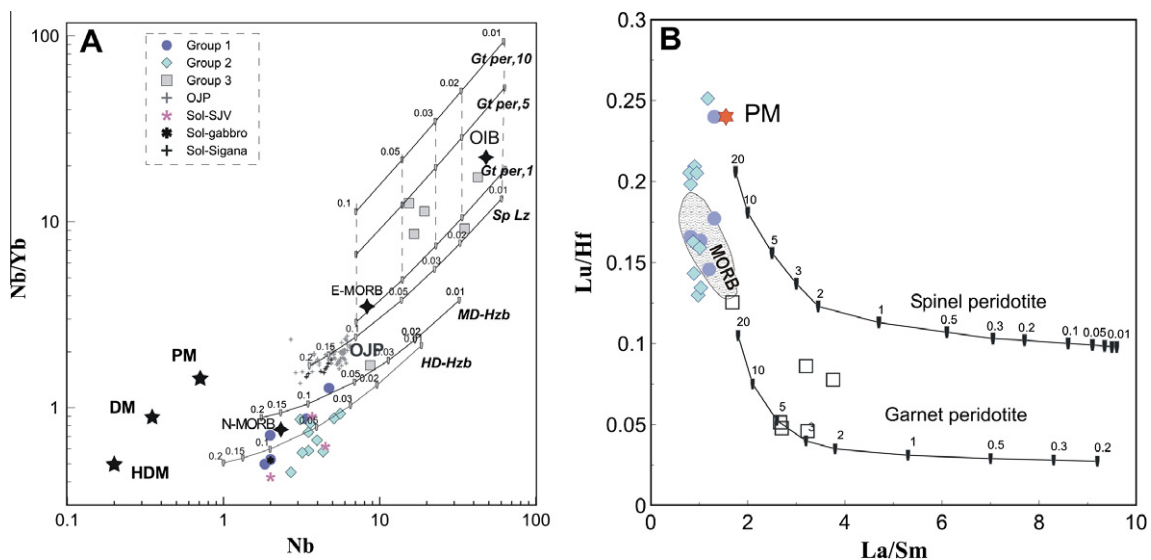

Fig. 12. Melting modeling. (A) Nb versus Nb/Yb. Curves are calculated melting curves for spinel lherzolite (Sp Lz), moderate-depleted harzburgite (MD-Hzb), high-depleted harzburgite (HD-Hzb), garnet peridotite containing 1%, 5% and 10% of garnet (Gt per. 10; for details see text, Section 6.4, and Table 5). Numbers denote degree of melting (non-modal batch melting, partition coefficients from Johnson (1998) and Bédard (1994)). The Nb concentration is weakly dependent on source composition, but varies with degree of melting. Nb/Yb ratios are governed by the modal composition of the source. DM – depleted mantle; HDM – high-depleted mantle. Other abbreviations see in Fig. 11. The data for the Solomon arc are from Tejada et al. (1996). (B) Lu/Hf versus La/Sm. The curves are taken from Regelous et al. (2003) and show the effect of the equilibrium melting of spinel and garnet peridotites between 0.01% and 20%. The source (star) has primitive mantle composition (Sun and McDonough, 1989). The enriched lavas (Group 3) are mixtures of spinel and garnet peridotite melts formed at low to medium degrees of melting. The depleted and transitional lavas (Groups 1 and 2) have low La/Sm and high Lu/Hf ratios which are indicative of even higher degrees of melting within the spinel stability field.

Table 5
Parameters of mantle sources and their compositions used for melting modeling.

Initial source					Melt						
Ol	Opx	Cpx	Sp	Gr	Ol	Opx	Cpx	Sp	Gr		
57	25	16	2	0	−7	25	80	2	0	Spinel lherzolite	Woodhead et al. (1993)
60	20	10	0	10	4	−19	105	0	10	Garnet peridotite	Johnson (1998)
83	15	0	2	0	35	63	0	2	0	Depleted harzburgite	Kelemen (1990)
80	17	2	1	0	32	65	2	1	0	Mantle wedge harzburgite	Parkinson and Pearce (1998)

The melting assumed Rayleigh fractionation with partition coefficients from Johnson (1998) for garnet and clinopyroxene and from Bédard (1994) for other minerals. Clinopyroxene is out after 20% and 24% of melting in spinel lherzolite and harzburgite, respectively. Garnet is out after 10% melting. The negative values refer to phases that do not participate in the melting reaction. Their relative portion in the residual source increases.

diagram (Fig. 12B) shows the melting curves for spinel and garnet peridotite, which parameters were borrowed from (Regelous et al., 2003). The basalts of Groups 1 and 2 clearly plot within the MORB field, whereas the OIB-type varieties (Group 3) are likely to be derived from mixed melts of spinel and garnet peridotite sources. Similar to the Nb–Yb systematics (Fig. 12B), the low La/Sm and high Lu/Hf ratios of the MORB-type basalts require large degrees of melting within the spinel stability field, of a source with lower La/Sm than primitive mantle. Alternatively, the OIB-type basalts likely formed at lower degrees of partial melting (2–5%) in both the spinel and garnet stability fields.

6.4. Mantle sources

Groups 1 and 2 have many geochemical features in common. They show similar MgO versus major and trace element correlations (Fig. 8), depletion in the LREE in the REE patterns and in Nb with respect to La in the multi-element patterns of (Fig. 9B and D) as well as Nb/Yb and Sm–Nd isotope systematics (Figs. 10 and 12A). The results of melting modeling (Section 6.4) also allow the assumption of a common parental magma for most of the volcanic rocks of Groups 1 and 2. However, other major (TiO_2, P_2O_5), medium rare earths (Nd, Sm, ΣREE, La/Yb_n), and trace-element (Y, Zr, Hf) characteristics (Table 3) require additional processes to have taken place during their genesis.

Group 1 basalts (MORB-type) have lower concentrations of Ti, Y, Zr and Hf than Group 2 basalts (Table 3). The REE characteristics (La/Sm_n = 0.5–0.8, Gd/Yb_n = 1.0–1.4; Fig. 9A), isotope data ($\varepsilon Nd_{av.}$ = 6.3; Fig. 10A) and results of melting modeling (Fig. 12) suggest that Group 1 basalts were derived from a depleted mantle source, melted in the spinel stability field, at high degrees of melting (10–15%).

Group 2 basalts (transitional) have higher Ti and other HFSE, P_2O_5, MREE and Zr/Nb, but lower MgO than Group 1 basalts (Table 3). Similarly to Group 1 the flat REE patterns, low Gd/Yb_n ratios (1.1–1.2), La/Sm versus Lu/Hf and Nb versus Nb/Yb systematics suggest a depleted mantle source (Figs. 9b and 12). However, they melted at slightly lower degrees of melting (5–10%; Fig. 12A) and had a different history of crystallization including fractionation of clinopyroxene (Fig. 11D), which resulted in higher Ti and MREE. In addition, we suggest crystallization of amphibole, possibly on a final stage of basalt formation, which could result in higher TiO_2 (Bazylev et al., 1999), MREE and Zr increasing with decreasing MgO (Fig. 8G; Table 3), because these elements are partly compatible in this mineral.

Group 3 tholeiitic to alkaline basalts (OIB-type) are characterized by enrichment in most incompatible elements such as LREE, Ti, Nb and Th (Figs. 8, 9 and 12). They possess rather lower values of εNd (3.5–5.2), which are more typical of HIMU-type mantle sources (Fig. 10; Zindler and Hart, 1986; Hofmann, 1997). Along with high TiO_2 (2.1–3.8 wt.%) and enriched LREE (La/Sm_n = 1.7–2.4), the most prominent feature of the OIB-type basalts is the presence of Nb positive anomalies in the multi-element patterns (Fig. 9C and F). The increased Gd/Yb_n ratios (2.1–3.3) in most samples are indicative of garnet fractionation at their formation (>60 km), because the HREE are partially coherent in garnet (Hirschman and Stolper, 1996). For these basalts we suggest formation from a HIMU-type mantle source, melted at lower degrees of melting (1–5%) in the spinel lherzolite (Gd/Yb_n < 2) and garnet peridotite (Gd/Yb_n > 2) stability fields, with a probable content of garnet in the latter case between 1% and 5% (Fig. 12). The modeled spinel to garnet facies mantle sources (Fig. 12) and the wide variations of incompatible elements in the Char OIB-type basalts (Figs. 8 and 9) are suggestive of a heterogeneous mantle source. Such a source could be either a melted column of upper mantle material (depleted in incompatible elements) and its hosted mantle

heterogeneities (enriched in incompatible elements), or a mixture of melts derived from a non-depleted mantle source and from the upper mantle during their ascent.

Thus, we conclude that the basalts of Groups 1 and 2 formed from a similar depleted mantle source in the spinel stability field, but at high and medium degrees of melting, respectively, and had different histories of fractional crystallization. The basalts of Group 3 formed from a non-depleted (enriched) heterogeneous mantle source, in the spinel and garnet stability fields, at low degrees of melting.

6.5. Tectonic settings

The extremely complicated structure of the Char zone represents a mix of tectonic slivers of different geodynamic origin, including pre-Devonian (Tarbagatai) and post-Devonian (Zharma-Saur) island-arc terranes (e.g., Berzin et al., 1994; Buslov et al., 2001; Fig. 1). The Char oceanic fragments in places occur close to suprasubduction units, even as a kind of "piled" structure. They are usually poorly outcropped and clear contacts between rock units are rare (Fig. 4C). Geochemical evidence does not support the involvement of subduction material in the genesis of the basalts. Instead, the geological and geochemical data presented above strongly favor the oceanic origin of the Late Devonian–Early Carboniferous volcanogenic-sedimentary units of the Char zone. In this section we will specify tectonic settings of their formation based on the whole set of geological, geochemical and isotope data.

The tholeiitic basalts of Group 1 are associated with brown chert (see Section 2; Fig. 4C and D) and have aphyric to microdoleritic structures (Fig. 5A and B). Geochemically they are characterized by higher MgO and lower incompatible elements (HFSE, REE) and by a progressive decrease of concentrations from Sm to La in the REE patterns, which all is typical of modern MORBs. The isotopic features of Group 1 basalts suggest their derivation from DM mantle source (Tables 2 and 4; Figs. 8–10). Modeling showed that Group 1 basalts could form at high degrees of melting (5–15%) of the depleted mantle with minimal fractional crystallization en-route to the surface (Figs. 11 and 12). These basalts may be analogues of modern mid-oceanic ridge basalt. The low-Ti melts, which produced Group 1 basalts, probably formed during decompressional melting of upper mantle material at an oceanic ridge. Thus, the low-Ti basalts of the Char SSZ may represent a fragment of the Late-Devonian–Early Carboniferous oceanic crust.

Group 2 basalts have doleritic and microporphyric structures and are associated with chert (Fig. 4B), siliceous shale and mudstone, although no direct contacts with the latter have been found. This transitional group is geochemically and petrologically similar to the high-Ti basalts of the Malaita accretionary complex of the Solomon Islands (Tejada et al., 1996). These basalts, Char and Solomon, are very similar in the MgO versus major element plots, REE and multi-element patterns, Nb versus Zr/Nb and Nb/Yb diagrams (Figs. 8–12). The Malaita units are often compared with the basalts of the Ontong-Java Plateau, OJP (Hughes, 2004). But unlike most Archean to Cretaceous accreted oceanic plateaus, which are large slivers up to hundreds meters thick and several thousand kilometers long (e.g., Kerr, 2003), the Char transitional basalts are exposed over a distance of 100–150 km as small exposed fragments of basaltic units, up to several meters thick and tens meters long. Mann and Taira (2004) studied the convergent zone between the OJP and the Solomon Islands and evaluated that as much as 80% of the crustal thickness of the plateau is subducted and only 20% of it is preserved on the overriding plate by accretion processes. Therefore, we suggest that a major part of a Late Devonian oceanic plateau could have been eroded by subduction and later destroyed by strike-slip faulting.

However, Group 2 basalts of probably oceanic plateau origin differ from typical OJB by lower Nb (Figs. 11 and 12). The Nb depletion relative to La in the multi-element spectra and the variable $^{207}Pb/^{204}Pb$ (Figs. 9 and 10) may be indicative of endogenic contamination, which may take place under an oceanic plateau, where the degrees of melting are usually high and may result in involvement of a big amount of upper mantle depleted material, which contains less Nb compared to a plume-related mantle source (OIB). On the other hand, negative Nb anomalies may result from participation of sediments, contamination by continental crust or fractionation of Ti–magnetite, which all are typical of suprasubduction basalts. However, we decline their suprasubduction origin because of (i) high TiO_2, (ii) medium to low Th, (iii) medium to high P_2O_5, (iv) low LREE, (v) low Sr/Y (0.7–3.0 compared to a mean of 50 for normal arc magmas; GEOROC), (v) Nb enrichment relative to Th in several samples of Group 2 (Nb/Th$_{pm}$ = 1.2–1.8, and (vi) high positive εNd (Figs. 8–10; Table 2; Sections 6.2 and 6.3). Thus, based on geological and geochemical data we suggest that the Char high-Ti basalts of Group 2, which are similar to the high-Ti basalts of the Malaita accretionary complex, represent fragments of an oceanic plateau.

Group 3 basalts generally have aphyric and microporphyric structures and occur as small tectonic fragments of pillow lavas and lava flows, locally associated with OPS sediments, chert and limy sandstone/mudstone (Table 1; Section 2). They possess OIB-type geochemical features such as high TiO_2, enriched LREE and Nb, differentiated HREE and lower εNd (Figs. 8–10). Their Zr/Hf and Nb/Ta ratios are close to the respective mantle values of 36 and 16 found in many Phanerozoic and Cenozoic within-plate basalts (e.g., Kamber and Collerson, 2000, Table 2). A particular feature is the enrichment in Nb, which may fractionate from Th and LREE through subduction-induced dehydration and is brought into the lower mantle by the subducted oceanic slab (Saunders et al., 1988; McCulloch and Gamble, 1991; Brenan et al., 1994). Such signatures are thought to be diagnostic for hot spot or plume-related basalts of oceanic islands (e.g., Sun and McDonough, 1989; Hofmann, 1997) and, thus, may indicate that the Group 3 basalts formed in an intra-oceanic setting of oceanic island related to mantle plume or hot spot.

6.6. Geodynamic implications

As was mentioned above, the processes of fractional crystallization and partial melting similar to those discussed in Sections 6.2–6.4 played a major role in the formation of basaltic units in mid-oceanic ridges, oceanic plateaus and oceanic islands. We compared the geological and geochemical features of the Char basalts with those of the Malaita accretionary prism, exposed on the Santa Isabel and Malaita Islands, which is within the convergent zone between the Ontong-Java oceanic plateau and Solomon Islands (Neal et al., 1997; Hughes, 2004; Mann and Taira, 2004). The Malaita accretionary prism hosts recent (Cretaceous to Paleocene) analogues of MORB-type, transitional and OIB-type basalts of the Char SSZ. Both localities contain typical volcanogenic and sedimentary units of OPS: massive and pillowed tholeiitic basalt with chert and mudstone interbeds at the bottom (oceanic floor and base of seamounts), siliceous to calcareous mudstone and shale (slope facies of seamounts), and alkaline basalts associated with limestone (top of oceanic rises) (Fig. 13A).

The Malaita analogue of Group 1 basalts is the Older Series of Early Cretaceous age (~125 Ma), which is in the bottom of the OPS section (Hughes, 2004). It consists of MORB-type massive and pillowed basalts associated with pelagic chert and may represent a base of the OJP (Tejada et al., 1996). Similarly, we regard the Char MORB-type basalts (Group 1) as a lower part of the Char oceanic plateau (see Section 6.5; Fig. 13B).

The Malaita analogue of Char transitional basalts (Group 2) is the San Jorge volcanic unit of Early Paleogene age (~64 Ma; Tejada et al., 1996), which includes basalts and their associated chert and limestone (Hughes and Turner, 1977). Group 2 basalts are intriguingly similar to the high-Ti Sigana and San Jorge basalts, which probably formed at the peripheral parts of the OJP (Tejada et al., 1996), and, together with overlapping oceanic sediments they were obducted onto the overriding plate, whereas the major part of OJP basalts was subducted. More evidence for a oceanic plateau comes from the high-degree fractionation of pyroxene in Group 2 basalts (Section 6.2), which could be possible in intermediate chambers formed during its subduction, during which, however, the mantle sources was the same, i.e. depleted harzburgite. Such
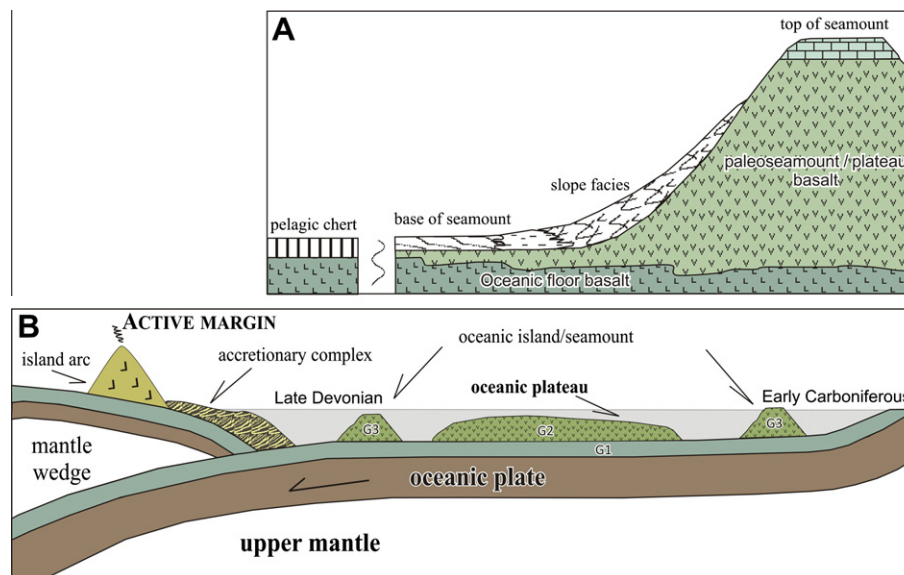

Fig. 13. (A) Schematic section through an oceanic seamount and its associated OPS (modified from Isozaki et al. (1990)). *Note*, sediment types change with deposition setting, i.e., carbonates at the top of the seamount, carbonate breccias, siliceous to calcareous mudstone, and shale on its slopes, siliceous shales, siliceous mudstones, and siltstones at its base/foothill, and cherts on the oceanic floor. (B) Speculative geodynamic setting for the formation of the Late Devonian–Early Carboniferous MORB-type (G1), OPB-type (G2) and OIB-type (G3) basalts of the Char suture-shear zone (for discussion see Section 6.6).

a specific setting of an accreted/obducted/subducted oceanic plateau was responsible for the formation of oceanic basalts that are enriched in Ti–Y–Hf–Th and depleted in LREE and Nb compared to Group 1 or MORB (Table 3). Thus, Group 2 basalts may represent a peripheral fragment of the Char oceanic plateau and they erupted onto the older oceanic lithosphere consisting of Char MORB-type basalts (Group 1).

The Malaita counterparts of Char OIB-type basalts (Group 3) are the Sigana Alkalic Suite (Late Cretaceous; ~89 Ma) and Younger Series (Paleocene; ~45 Ma) (Tejada et al., 1996). Both localities include basalt varieties that are variably enriched in incompatible elements, i.e., the Younger Series and the Sigana Alkalic Suite basalts in the Malaita complex (Tejada et al., 1996) and the Nikolaevka site and the Char site OIBs in the Char SSZ (Section 5.2; Fig. 2), respectively. It is quite possible that in both cases, the less enriched OIB-type basalts (Younger Series and Nikolaevka site) erupted over thinner and younger oceanic lithosphere and/or closer to mid-oceanic ridge than the more enriched basalts (Sigana and Char site), which erupted on thicker and older oceanic lithosphere (Regelous et al., 2003 and references therein). Such a bimodal distribution also has been described for the older (81–83 Ma) and younger (55–42 Ma) seamounts of the Emperor-Hawaii chain of seamounts (Regelous et al., 2003) and the older and younger paleoseamounts of the Paleo-Asian Ocean incorporated into accretionary complexes of Russian Altay (Safonova, 2008; Safonova et al., 2011a, 2011b). Taking into account the average velocity of oceanic subduction and the growth of the oceanic lithosphere thickness (e.g. Parsons and Sclater, 1977; Reid and Jackson, 1981), the age difference between the less and more enriched basalts erupted over one hot spot and within one oceanic plate may be about 30–50 Ma. This value is close to the time interval between the 89 Ma age of the Younger Series and the 44 Ma age of the Sigana Suite in the Malaita complex (Tejada et al., 1996) and between the micropaleontological age constrains of the Late Devonian (~380 Ma) Nikolaevka site OPS and Early Carboniferous (~340 Ma) Char site OPS (Section 2). In our case, the less enriched Nikolaevka site samples yielded 3–5% degree of melting, whereas the more enriched Char site varieties formed at 1–2% (Figs. 12A and 13).

Thus, the Char OIBs may represent hot-spot-related oceanic islands/seamounts, similar to the Malaita OIBs. Variably incompatible element enriched basalt varieties formed over the oceanic lithosphere of different age/thickness and were accreted to the respective active margins at different times, possibly before and after the accretion of the oceanic plateau (Group 2). The Nikolaevka site (Late Devonian) and the Char site (Early Carboniferous?) OIBs were possibly accreted before/after the accretion of the Char Late Devonian oceanic plateau.

7. Conclusions

The paper presents the first results of a comprehensive geochemical and petrological study of the Late Devonian–Early Carboniferous mafic volcanic rocks of the Char suture-shear zone in East Kazakhstan, which includes detailed analysis of their geological relations, chemical composition (major and trace elements, Sr and Nd isotopes) and petrogenesis of basaltic melts (fractional crystallization/melting modeling). Based on the whole set of geological, stratigraphic, petrologic and geochemical date, we concluded the following.

1. Three groups of oceanic basalts of Late Devonian–Early Carboniferous age coexist in the Char suture-shear zone. They are associated with Oceanic Plate Stratigraphy sediments, such as brown/radiolarian/ribbon chert, carbonate breccias, limy and siliceous sandstone/mudstone and reefal limestone.

2. Group 1 oceanic basalts are associated with oceanic siliceous sediments (chert) and are characterized by medium TiO_2, relatively flat REE patterns ($La/Sm_n = 0.7$, $Gd/Yb_n = 1.3$), Nb depletion in the multi-element spectra relative to La ($Nb/La_{pm} < 1$), $Zr/Nb_{av.} = 42$ and $\varepsilon Nd_{av.} = 6.3$. Group 1 basalts formed at high degrees of melting from a depleted mantle source with minimal fractional crystallization. They formed in a mid-oceanic ridge setting and represent a fragment of the Middle–Late Devonian oceanic crust of the Paleo-Asian Ocean.

3. Group 2 oceanic basalts are associated with both chert and carbonate and possess geochemical features partly similar to those of Group 1 basalts, but with higher TiO_2, Hf, Y, Zr and P_2O_5. They are also characterized by low Nb ($Nb/La_{pm} < 1$) and flat REE patterns ($La/Sm_n = 0.6$, $Gd/Yb_n = 1.1$), $\varepsilon Nd_{av.} = 8.3$, and $Zr/Nb = 44$. Group 2 basalts formed under lower degrees of melting compared to Group 1, but also from a depleted mantle source and, possibly, experienced fractionation of clinopyroxene. They represent a peripheral part of the Char plateau, which existed in the Paleo-Asian Ocean in Late Devonian time.

4. Group 3 oceanic basalts associated with lime mudstone and carbonate breccias. They are enriched in incompatible elements, i.e. have high LREE ($La/Sm_n = 1.8$), differentiated HREE ($Gd/Yb_n = 2.3$), Nb positive anomalies in the multi-element diagrams ($Nb/Th_{pm} = 1.5$, $Nb/La_{pm} = 1.1$), and possess low Zr/Nb ratio (~9) and lower $\varepsilon Nd_{av.} = 4.6$. Compared to Groups 1 and 2, Group 3 basalts originated at lower degrees of melting, from a heterogeneous mantle source in the spinel ($Gd/Yb_n < 2$) and garnet ($Gd/Yb_n > 2$) stability fields and also experienced fractionation of clinopyroxene. The basalts formed in plume-related oceanic island setting and represent two oceanic islands formed over the oceanic lithosphere of the Paleo-Asian Ocean in the Late Devonian and Early Carboniferous.

References

Albarède, F., 1995. Introduction to Geochemical Modeling. Cambridge University Press, Cambridge.

Arndt, N.T., Jenner, G.A., 1986. Crustally contaminated komatiites and basalts from Kambalda, Western Australia. Chemical Geology 56, 229–255.

Badarch, G., Cunningham, W.D., Windley, B.F., 2002. A new terrane subdivision for Mongolia: implications for the Phanerozoic crustal growth of Central Asia. Journal of Asian Earth Sciences 21, 87–110.

Bazylev, B.A., Silantyev, S.A., Kononkova, N.N., 1999. Phlogopite and hornblende in spinel harzburgites from the Mid-Atlantic Ridge: mineral assemblages and origin. Ofioliti 24, 59–60.

Bédard, J.H., 1994. A procedure for calculating the equilibrium distribution of trace elements among the minerals of cumulate rocks, and the concentration of trace elements in the coexisting liquids. Chemical Geology 118, 143–153.

Belyaev, S. Yu, 1985. Tectonics of Chara Zone (East Kazakhstan). IGiG SO AN SSSR, Novosibirsk (in Russian).

Berzin, N.A., Coleman, R.G., Dobretsov, N.L., Zonenshain, L.P., Xiao, Xuchang, Chang, E.Z., 1994. Geodynamic map of the western part of the Paleoasian Ocean. Russian Geology and Geophysics 35, 5–22.

Brenan, J.M., Shaw, H.F., Phinney, D.L., Ryerson, F.J., 1994. Rutile-aqueous fluid partitioning of Nb, Ta, Hf, Zr, U and Th: implications for high-field strength element depletions in island-arc basalts. Earth and Planetary Science Letters 128, 327–339.

Buslov, M.M., Fujiwara, Y., Iwata, K., Semakov, N.N., 2004a. Late Paleozoic–Early Mesozoic geodynamics of Central Asia. Gondwana Research 7, 791–808.

Buslov, M.M., Safonova, I.Yu., Watanabe, T., Obut, O., Fujiwara, Y., Iwata, K., Semakov, N.N., Sugai, Y., Smirnova, L.V., Kazansky, A.Yu., 2001. Evolution of the Paleo-Asian Ocean (Altai-Sayan region, Central Asia) and collision of possible Gondwana-derived terranes with the southern marginal part of the Siberian continent. Geosciences Journal 5, 203–224.

Buslov, M.M., Watanabe, T., Fujiwara, Y., Iwata, K., Smirnova, L.V., Safonova, I.Yu., Semakov, N.N., Kiryanova, A.P., 2004b. Late Paleozoic faults of the Altai region, Central Asia: tectonic pattern and model of formation. Journal of Asian Earth Sciences 23, 655–671.

Bykova, M.S., Kushev, G.L., 1974. Unsolved question of Carboniferous stratigraphy in East Kazakhstan. In: Stratigraphy of the Devonian, Carboniferous and Permian in Kazakhstan. Nauka KazSSR Publ., Alma-Ata, pp. 73–79.

Didenko, A.N., Mossakovskiy, A.A., Pecherskiy, D.M., Ruzhentsev, S.G., Samygin, S.G., Kheraskova, T.N., 1994. Geodynamics of Paleozoic oceans of Central Asia. Russian Geology and Geophysics 35, 48–62.

Dobretsov, N.L., Berzin, N.A., Buslov, M.M., 1995. Opening and tectonic evolution of the Paleo-Asian Ocean. International Geology Review 35, 335–360.

Dobretsov, N.L., 2003. Evolution of structures of the Urals, Kazakhstan, Tien Shan, and Altai-Sayan region within the Ural-Mongolian fold belt (Paleoasian ocean). Russian Geology and Geophysics 44, 3–26.

Ermolov, P.V., Dobretsov, N.L., Polyansky, N.V., Klenina, N.L., Khomyakov, V.D., Kuzebny, V.S., Revyakin, P.S., Bortsov, V.D., 1981. Ophiolites of the Chara zone. In: Abdulin, A.A., Patalakha, E.I. (Eds.), Ophiolites. Nauka KazSSR, Alma-Ata, pp. 103–178 (in Russian).

Floyd, P.A., Winchester, J.A., 1975. Magma-type and tectonic setting discrimination using immobile elements. Earth and Planetary Science Letters 27, 211–218.

Fowler, A.D., Jensen, L.S., 1989. Quantitative trace element modeling of the crystallization history of the Kinojevis and Blake River groups, Abitibi greenstone belt, Ontario. Canadian Journal of Earth Sciences 26, 1356–1365.

Glory, S., De Grave, J., Buslov, M.M., Zhimulev, F.I., Izmer, A., Vandoome, W., Ryabinin, A., Van de haute, P., Vanhaecke, F., Elburg, M.A., 2011. Formation and Palaeozoic evolution of the Gorny-Altai-Mongolia suture zone (South Siberia): zircon U/Pb constraints on the igneous record. Gondwana Research 20, 465–484.

Haase, K.M., 2002. Geochemical constrains on magma sources and mixing processes in Easter Microplate MORB (SE Pacific): a case study of plume–ridge interaction. Chemical Geology 182, 335–355.

Hirschman, M.M., Stolper, E.M., 1996. A possible role for garnet pyroxenite in the origin of the "garnet signature" in MORB. Contributions to Mineralogy and Petrology 124, 185–208.

Hofmann, A.W., 1988. Chemical differentiation of the Earth: the relationship between mantle, continental crust, and oceanic crust. Earth and Planetary Science Letters 90, 297–314.

Hofmann, A.W., 1997. Mantle geochemistry: the message from oceanic volcanism. Nature 385, 219–229.

Hughes, G.W., 2004. Accretion of the Ontong Java plateau to the Solomon arc: a historical perspective. Tectonophysics 389, 127–136.

Hughes, G.W., Turner, C.C., 1977. Upraised Pacific Ocean floor, southern Malaita, Solomon Islands. Geological Society of America Bulletin 88, 412–424.

Humphris, S.E., Thompston, G., 1978. Hydrothermal alteration of oceanic basalts by seawater. Geochimica et Cosmochimica Acta 42, 107–125.

Isozaki, Y., Maruyama, Sh., Fukuoka, F., 1990. Accreted oceanic materials in Japan. Tectonophysics 181, 179–205.

Isozkai, Y., Aoki, K., Nakama, T., Yanai, S., 2010. New insight into a subduction-related orogen: a reappraisal of the geotectonic framework and evolution of the Japanese Islands. Gondwana Research 18, 82–105.

Iwata, K., Obut, O.T., Buslov, M.M., 1997. Devonian and Lower Carboniferous radiolaria from the Chara ophiolite belt, East Kazakhstan. News of Osaka Micropaleontologist 10, 27–32.

Iwata, K., Watanabe, T., Akiyama, M., Dobretsov, N.L., Belyaev, S.Yu., 1994. Paleozoic microfossils of the Chara Belt in Eastern Kazakhstan. Russian Geology and Geophysics 35, 125–130.

Jacobsen, S.B., Wasserburg, G.J., 1984. Sm–Nd evolution of chondrites and achondrites. Earth Planetary Science Letters 67, 137–150.

Jenner, G.A., Longerich, H.P., Jackson, S.E., Fryer, B.J., 1990. ICP-MS – a powerful tool for high precision trace element analysis in earth sciences: evidence from analysis of selected U.S.G.S. reference samples. Chemical Geology 83, 133–148.

Jensen, L.S., 1976. A new cation plot for classifying subalkalic volcanic rocks – Ontario Division Mines Misc., 66.

Jochum, K.P., Nohl, U., 2008. Reference materials in geochemistry and environmental research and the GeoReM database. Chemical Geology 253, 50–53.

Johnson, K.T.M., 1998. Experimental determination of partition coefficients for rare earth and high-field-strength elements between clinopyroxene, garnet, and basaltic melt at high pressure. Contributions to Mineralogy and Petrology 133, 60–68.

Kamber, B.S., Collerson, K.D., 2000. Zr/Nb systematics of ocean island basalts reassessed – the case for binary mixing. Journal of Petrology 41, 1007–1021.

Kelemen, P.B., 1990. Reaction between ultramafic rock and fractionating basaltic magma I. Phase relations, the origin of calc-alkaline magma series, and the formation of discordant dunite. Journal of Petrology 31, 51–98.

Kerr, A.C., 2003. Oceanic plateaus. In: Rudnick, R.L. (Ed.), The Crust. Holland, H.G., Turekian, K.K. (Eds.), Treatise on Geochemistry. Elsevier–Pergamon, Oxford, pp. 537–566 (Chapter 3).

Kröner, A., Windley, B., Badarch, G., Tomurtogoo, O., Hegner, E., Jahn, B.M., Gruschka, S., Khain, E.V., Demoux, A., Wingate, M.T.D., 2007. Accretionary growth and crust formation in the Central Asian orogenic belt and comparison with the Arabian-Nubian shield. In: Hatcher, R.D., Jr., Carlson, M.P., McBride, J.H., Martinez Catalan, J.R. (Eds.), Framework of Continental Crust, vol. 200. Geological Society of America, Memoir, pp. 181–209.

Kröner, A., Alexeiev, D.V., Hegner, E., Rojas-Agramonte, Y., Corsini, M., Chao, Y., Wong, J., Windley, B.F., Liu, D., Tretyakov, A.A., 2011. Zircon and muscovite ages, geochemistry, and Nd–Hf isotopes for the Aktyuz metamorphic terrane: evidence for an Early Ordovician collisional belt in the northern Tianshan of Kyrgyzstan. Gondwana Research. doi:10.1016/j.gr.2011.05.010.

Le Maitre, R.W., Streckeisen, A., Zanettin, B., Le Bas, M.J., Bonin, B., Bateman, P., Bellieni, G., Dudek, A., Efremova, S., Keller, J., Lamere, J., Sabine, P.A., Schmid, R., Sorensen, H., Woolley, A.R., 2002. Igneous Rocks: A Classification and Glossary of Terms, Recommendations of the International Union of Geological Sciences, Subcommission of the Systematics of Igneous Rocks. Cambridge University Press.

Li, J.Y., 1995. Main characteristics and emplacement processes of the East Junggar ophiolites, Xinjiang, China. Acta Petrologica Sinica 11 (Suppl.), 73–84.

Li, J.-Y., 2006. Permian geodynamic setting of Northeast China and adjacent regions: closure of the Paleo-Asian Ocean and subduction of the Paleo-Pacific Plate. Journal of Asian Earth Sciences 26, 207–224.

Li, Xian-Hua, Li, Zheng-Xiang, Zhou, Hanwen, Liu, Ying, Kinny, Peter D., 2002. U–Pb zircon geochronology, geochemistry and Nd isotopic study of Neoproterozoic bimodal volcanic rocks in the Kangdian Rift of South China: implications for the initial rifting of Rodinia. Precambrian Research 113, 135–154.

Mann, P., Taira, A., 2004. Global tectonic significance of the Solomon Islands and Ontong Java Plateau convergent zone. Tectonophysics 389, 137–190.

McCulloch, M.T., Gamble, A.J., 1991. Geochemical and geodynamical constraints on subduction zone magmatism. Earth and Planetary Science Letters 102, 358–374.

Miyashiro, A., 1973. The Troodos ophiolitic complex was probably formed in an island arc. Earth and Planetary Science Letters 19, 218–224.

Neal, C.R., Mahoney, J.J., Kroenke, L.W., Duncan, R.A., Petterson, M.G., 1997. The Ontong Java Plateau. In: Mahoney, J.J., Coffin, M.F. (Eds.), Large Igneous Provinces: Continental, Oceanic, and Planetary Flood Magmatism. American Geophysical Union Monograph 100, Washington, DC, pp. 183–216.

Orihashi, Y., Hirata, T., 2003. Rapid quantitative analysis of Y and REE abundances in XRF glass bead for selected GSJ reference rock standards using Nd-YAG 266 nm UV laser ablation ICP-MS. Geochemical Journal 37, 401–412.

Parkinson, I.J., Pearce, J.A., 1998. Peridotites from the Izu-Bonin-Mariana forearc (ODP Leg 125): evidence for mantle melting and melt-mantle interaction in a supra-subduction zone setting. Journal of Petrology 39 (9), 1577–1618.

Parsons, B., Sclater, J.G., 1977. An analysis of the variation of ocean floor bathymetry and heat flow with age. Journal of Geophysical Research 82, 803–827.

Pearce, J.A., Peate, D.W., 1995. Tectonic implications of the composition of volcanic arc magmas. Annual Reviews in Earth and Planetary Sciences 23, 251–285.

Pfander, J.A., Jochum, K.P., Kozakov, I., Kröner, A., Todt, W., 2002. Coupled evolution of back-arc and island arc-like mafic crust in the late-Neoproterozoic Agardagh Tes-Chem ophiolite, Central Asia: evidence from trace element and Sr–Nd–Pb isotope data. Contributions to Mineralogy and Petrology 143, 154–174.

Phedorin, M.A., Bobrov, V.A., Chebykin, E.P., Goldberg, E.L., Melgunov, M.S., Filippova, S.V., Zolotarev, K.V., 2000. Comparison of synchrotron radiation X-ray fluorescence with conventional techniques for the analysis of sedimentary samples. Geostandards Newsletter: The Journal of Geostandards and Geoanalysis 24, 205–216.

Polat, Al., Kerrich, R., Wyman, D., 1999. Geochemical diversity in oceanic komatiites and basalts from the late Archean Wawa greenstone belts, Superior Province, Canada: trace element and Nd isotope evidence for a heterogeneous mantle. Precambrian Research 94, 139–173.

Polyanskii, N.V., Dobretsov, N.L., Ermolov, P.V., Kuzebnyi, V.S., 1979. The structure and history of the Char ophiolite belt. Russian Geology and Geophysics 16, 52–62.

Redman, B.A., Keays, R.R., 1985. Archean volcanism in the eastern Goldfields Province, Western Australia. Precambrian Research 30, 113–152.

Reid, I., Jackson, H.R., 1981. Oceanic spreading rate and crustal thickness. Marine Geophysical Researches 5, 165–172.

Regelous, M., Hofmann, A.W., Abouchami, W., Galer, S.J.G., 2003. Geochemistry of Lavas from the Emperor Seamounts, and the Geochemical evolution of Hawaiian Magmatism from 85 to 42 Ma. Journal of Petrology 44, 113–140.

Rojas-Agramonte, Y., Kröner, A., Demoux, A., Xia, X., Wang, W., Donskaya, T., Liu, D., Sun, M., 2011. Detrital and xenocrystic zircon ages from Neoproterozoic to Palaeozoic arc terranes of Mongolia: significance for the origin of crustal fragments in the Central Asian Orogenic Belt. Gondwana Research 19, 751–763.

Romer, R.L., Hahne, K., 2010. Life of the Rheic Ocean: scrolling through the shale record. Gondwana Research 17, 236–253.

Romer, R.L., Heinrich, W., Schröder-Smeibidl, B., Meixner, A., Fischer, C.-O., Schulz, C., 2005. Elemental dispersion and stable isotope fractionation during reactive fluid-flow and fluid immiscibility in the Bufa del Diente aureole, NE-Mexico: evidence from radiographies and Li, B, Sr, Nd, and Pb isotope systematics. Contributions to Mineralogy and Petrology 149, 400–429.

Ryazantsev, A.V., 1994. Ophiolites of the Bayanhongor zone in the Paleozoic structure of Mongolia. Doklady of the Russian Academy of Sciences 336, 651–654 (in Russian).

Safonova, I.Yu., Buslov, M.M., Iwata, K., Kokh, D.A., 2004. Fragments of Vendian–Early Carboniferous oceanic crust of the Paleo-Asian Ocean in foldbelts of the Altai-Sayan region of Central Asia: geochemistry, biostratigraphy and structural setting. Gondwana Research 7, 771–790.

Safonova, I.Yu., 2008. Geochemical evolution of the Paleo-Asian Ocean intra-plate magmatism from the Late Neoproterozoic to the Early Cambrian. Petrology 16, 492–511.

Safonova, I.Yu., Simonov, V.A., Buslov, M.M., Ota, T., Maruyama, Sh., 2008. Neoproterozoic basalts of the Paleo-Asian Ocean (Kurai accretion zone, Gorny Altai, Russia): geochemistry, petrogenesis, geodynamics. Russian Geology and Geophysics 49, 254–271.

Safonova, I.Yu., 2009. Intraplate magmatism and oceanic plate stratigraphy of the Paleo-Asian and Paleo-Pacific Oceans from 600 to 140 Ma. Ore Geology Reviews 35, 137–154.

Safonova, I.Yu., Utsunomiya, A., Kojima, S., Nakae, S., Tomurtogoo, O., Filippov, A.N., Koizumi, K., 2009. Pacific superplume-related oceanic basalts hosted by accretionary complexes of Central Asia, Russian Far East and Japan. Gondwana Research 16, 587–608.

Safonova, I.Yu., Buslov, M.M., Simonov, V.A., Izokh, A.E., Komiya, T., Kurganskaya, E.V., Ohno, T., 2011a. Geochemistry, petrogenesis and geodynamic origin of basalts from the Katun' accretionary complex of Gorny Altai (southwestern Siberia). Russian Geology and Geophysics 52, 421–442.

Safonova, I.Yu., Sennikov, N.V., Komiya, T., Bychkova, Y.V., Kurganskaya, E.V., 2011b. Geochemical diversity in oceanic basalts hosted by the Zasur'ya accretionary complex, NW Russian Altai, Central Asia: implications from trace elements and Nd isotopes. Journal of Asian Earth Sciences 42, 191–207.

Santosh, M., 2010. A synopsis of recent conceptual models on supercontinent tectonics in relation to mantle dynamics, life evolution and surface environment. Journal of Geodynamics 50, 116–133.

Santosh, M., Maruyama, S., Sato, K., 2009. Anatomy of a Cambrian suture in Gondwana: Pacific-type orogeny in southern India? Gondwana Research 16, 321–341.

Saunders, A.D., Norry, M.J., Tarney, J., 1988. Origin of MORB and chemically-depleted mantle reservoirs: trace element constrains. Journal of Petrology (Special Lithosphere Issue), 415–455.

Seltmann, R., Soloviev, S., Shatov, V., Pirajno, F., Naumov, E., Cherkasov, S., 2010. Metallogeny of Siberia: tectonic, geologic and metallogenic settings of selected significant deposits. Australian Journal of Earth Sciences 57, 655–706.

Sengör, A.M.C., Natal'in, B.A., Burtman, V.S., 1993. Evolution of the Altaid tectonic collage and Paleozoic crustal growth in Asia. Nature 364, 299–307.

Sengör, A.M.C., Natal'in, B.A., 1996. Palaeotectonics of Asia: fragments of a synthesis. In: Yin, A., Harrison, M. (Eds.), Tectonic Evolution of Asia. Cambridge University Press, Cambridge, pp. 486–640.

Sennikov, N.V., Iwata, K., Ermikov, V.D., Obut, O.T., Khlebnikova, T.V., 2003. Oceanic sedimentation settings and fauna associations in the Paleozoic on the southern framing of the West Siberian Plate. Russian Geology and Geophysics 44, 156–171.

Sun, S., McDonough, W.F., 1989. Chemical and isotopic systematics of oceanic basalts: implications for mantle composition and processes. In: Saunders, A.D., Norry, M.J. (Eds.), Magmatism in the Ocean Basins, vol. 42. Special Publication, London, pp. 313–345 (Journal of the Geological Society).

Taylor, S.T., McLennan, S.M., 1985. The Continental Crust: Composition and Evolution. Blackwell, Oxford, 312 pp.

Tejada, M.L.G., Mahoney, J.J., Duncan, R.A., Hawkins, M.P., 1996. Age and geochemistry of basement and Alkalic Rocks of Malaita and Santa Isabel, Solomon Islands, Southern Margin of Ontong Java Plateau. Journal of Petrology 37, 361–394.

Thompson, G., 1991. Metamorphic and hydrothermal processes: basalt–seawater interactions. In: Floyd, P.A. (Ed.), Oceanic Basalts. Blachie and Sons Ltd., Glasgow, pp. 148–173.

Valsami-Jones, E., Ragnarsdottir, K.V., 1997. Controls on uranium and thorium behaviour in ocean-floor hydrothermal systems: examples from the Pindos ophiolite, Greece. Chemical Geology 135, 263–274.

Winchester, J.A., Floyd, P.A., 1977. Geochemical discrimination of different magma series and their differentiation products using immobile elements. Chemical Geology 20, 325–343.

Windley, B.F., Alexeiev, D., Xiao, W., Kröner, A., Badarch, G., 2007. Tectonic models for accretion of the Central Asian Orogenic Belt. Journal of the Geological Society, London 164, 31–47.

Woodhead, J., Eggins, S., Gamble, J., 1993. High field strength and transition element systematics in island arc and back-arc basin basalts: evidence for multi-phase melt extraction and a depleted mantle wedge. Earth and Planetary Science Letters 114, 491–504.

Xiao, W.J., Huang, B.C., Han, C.M., Sun, S., Li, J.L., 2010. A review of the western part of the Altaids: a key to understanding the architecture of accretionary orogens. Gondwana Research 18, 253–273.

Xiao, W.J., Windley, B.F., Hao, J., Zhai, M.G., 2003. Accretion leading to collision and the Permian Solonker suture, Inner Mongolia, China: termination of the central Asian orogenic belt. Tectonics 22, 1069. doi:10.1029/2002TC001484.

Yakubchuk, A., 2004. Architecture and mineral deposit settings of the Altaid orogenic collage: a revised model. Journal of Asian Earth Sciences 23, 761–779.

Zartman, R.E., Doe, B.R., 1981. Plumbotectonics – the model. In: Zartman, R.E., Taylor, S.R. (Eds.), Evolution of the Upper Mantle, vol. 75, pp. 135–162 (Tectonophysics).

Zindler, A., Hart, S., 1986. Chemical geodynamics. Annual Reviews in Earth and Planetary Science 14, 493–571.

Zonenshain, L.P., Kuzmin, M.I., Natapov, L.M., 1990. Geology of the USSR: a plate tectonic synthesis. Geodynamic Series, vol. 21. American Geophysical Union, Washington, DC, 242 pp.